Satellite Orbit Errors and Their Influence on Interferograms
Diploma Thesis

Ing. Ivana Čapková
Department of Mapping and Cartography
Faculty of Civil Engineering
Czech Technical University, Prague
Supervisor: Doc. Ing. Lena Halounová, CSc.

Prohlášení

Závazně prohlašuji, že jsem diplomovou práci vypracovala samostatně a uvedla všechny použité zdroje.

V Praze 30. května 2005

Ivana Čapková

Anotace

Diplomová práce se zabývá radarovou interferometrií a chybami drah družic, jejichž data se používají pro interferometrické účely, tj. ERS-1/2 a ENVISAT. Zabývá se přesností drah družic a analyzuje vliv chyb v drahách na interferogramy pro různé způsoby, jak vytvořit interferogram (s odečtenou topografií). Tento vliv je také číselně vyhodnocen.

Kromě toho diplomová práce obsahuje přehled metod na opravu drah družic založených na reziduální fázi interferogramu a analyzuje je.

Abstract

The thesis deals with SAR interferometry and orbit errors of the satellites whose data are used for interferometric purposes, i.e. ERS-1/2 and ENVISAT. The precision of the orbits is discussed and the influence of the orbit errors on the interferograms is analysed for various means of (topography-free) interferogram creation. The influence is also evaluated numerically.

In addition, various methods for baseline adjustment based on the number of residual fringes are reviewed and analysed.

Contents

Acknowledgements

The ERS data used was granted by ESA Cat-1 project. For interferometric processing, the open-source software DORIS and DEOS precise orbits were used.

I would also like to thank to Doc. Ing. Lena Halounová, CSc. and Ján Kianička for a careful review of the thesis and moral support.

Chapter 1

Introduction

Radar interferometry is one of the methods used in remote sensing. It serves for two basic applications: digital elevation model (DEM) creation, or deformation (subsidences, landslides) mapping. However, the interferogram is corrupted by other influences: atmospheric delay or orbit errors. Both of these influences have a long-wave character and cannot be separated from each other.

The interferogram is created by subtracting the phase of two radar scenes of the same area. It does not matter if the two scenes are acquired by the same satellite or by two different satellites. After subtracting the phase of the flat Earth, the interferogram contains a topographic signal, which is either extracted (for DEM creation) or subtracted (for deformation mapping applications).

All of these computations depend on the positions of the two satellites. We usually use precise orbits with accuracy of the order of 10 cm, but it looks like this is not accurate enough. In addition to the fact that the scene is shifted by more than one hundred meters, there are residual fringes in interferograms after topography subtraction, which means that the extracted DEM is sloped.

On the other hand, if we use an external DEM to subtract the topographic signal, it is often shifted with respect to the interferogram, causing additional errors.

After topography subtraction, the resulting image should be plain-coloured (i.e. the phase should have the same value in the entire area) except for the places of deformations. In our applications, this is never the case. The image has some fringes (from half to two, depending on several factors), which we attribute to orbit errors and atmospheric delay. These residual fringes should be eliminated in order to get a "correct" interferogram: it does not matter if they are really caused by an orbit error or by atmospheric delay. We need to find "correct" orbit positions, which help generate the "correct" interferogram.

Although the residual fringes can be only seen in a "topography-free" interferogram, the information may be also used for DEM extraction applications, if there is a DEM of the area available (although scarce or less precise).

The accuracy of precise satellite orbits is different in different directions. The inaccuracy in each direction may influence the interferogram in a different way.

This thesis is aimed at analysis of the orbit error influence on interferograms. It also deals with the ways of obtaining the precise orbits and the tracking systems onboard

ERS-1/2 and ENVISAT satellites. In addition, it also cites some methods of eliminating the orbit-error influence and procedures for adjusting the orbits.

The orbit error influence can be easily distinguished from deformation influences. However, the orbit errors make the interferogram look sloped, and the deformation spots often cannot be recognized.

Therefore, we are not interested much in the influence of orbit error on scene shift; we would rather like to find the way how to eliminate the "orbital" fringes from the interferogram, making the deformation spots more easily visible.

Chapter 2

Radar Interferometry

Radar interferometry is a method of processing a pair of radar scenes (either from airplane, or a satellite) in order to get a digital elevation model (DEM). Besides that, it can be used for Earth deformation (subsidences, landslides) monitoring or atmosphere monitoring.

For a conventional interferometric processing, two radar scenes are needed. In comparison to other remote sensing techniques, radar interferometry takes advantage not only of the magnitude of the signal, but also of the signal phase. While the signal magnitude corresponds to the reflectivity of the ground, the phase φ corresponds to the distance D between the satellite and the reflector which is

$$D = n \cdot \lambda + \varphi \frac{\lambda}{2\pi} \tag{2.1}$$

where n is an integer ambiguity and λ is the radar wavelength.

The interferometric processing uses the reflectivity information only for coregistration of the images; for DEM creation, deformation mapping and exploring the atmosphere, only the phase information is used.

2.1 Basic Terms

In interferometry, two satellite scenes are used, no matter whether acquired by two satellites or by one satellite in different passes. Let us call one of the scene *master* and the other one *slave*. The results are then related to the master scene.

The distance between the satellites in the moment of acquisiton of the scenes is called spatial *baseline* B (it can vary throughout the image, if the satellite tracks are not exactly parallel). The baseline is always perpendicular to the track [28]. We recognize the *perpendicular baseline* $B_\perp$ and *parallel baseline* $B_\parallel$, i.e. perpendicular and parallel to the radar ray transmitted towards the Earth.

Let us emphasize here that radar does not acquire the scenes perpendicular to the Earth surface — the *look angle* Θ (the angle between the Earth normal and radar ray) is 16 – 21 °. This allows the images to have better resolution than they would have in the case of perpendicular view. On the other hand, *incidence angle* $(\Theta + \varepsilon)$ is the angle between

the Earth normal and radar ray at the place where the ray reaches the ground (see figure 2.1. The difference between the angles $\varepsilon \approx 4°$ for ERS.

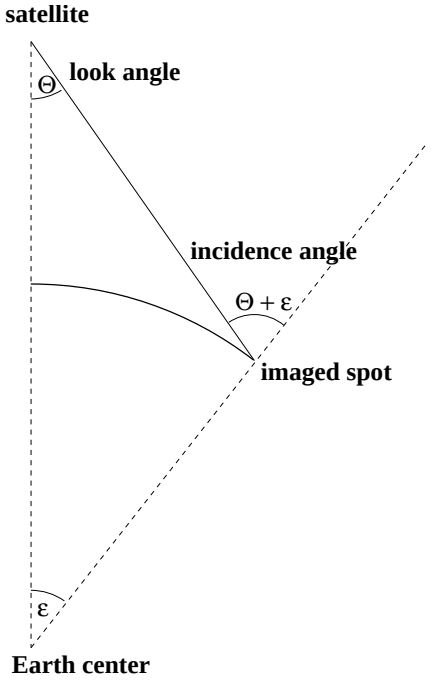

Figure 2.1: The difference between the look and incidence angle.

Another important term in interferometry is the *temporal baseline*, i.e. the temporal difference between acquisitions of the two scenes. The longer the temporal baseline, the more decorrelated the area may get — water surfaces get decorrelated in fractions of seconds, forested or otherwise vegetated areas get decorrelated in seconds. Agricultural fields may get decorrelated in days or weeks (if farmed). Residential areas are the most stable.

Another important term is the *height ambiguity*. As mentioned above, the phase value is ambiguous, and so is the height of the reflector computed out of the phase. Height ambiguity is the height difference corresponding to one phase fringe, i.e. 2π radians. The derivation of height ambiguity value will be described in section 2.3.

Let us also mention the resolution of the image. We can resolve two directions: *azimuth* direction is parallel to the satellite track, while *range* direction is perpendicular to it. The resolution of the acquired scene is approx. 4.5 m in the azimuth direction and 20–30 m in the range direction. Due to the radar acquisiton geometry, the resolution in the range direction changes throughout the image, being better at far range.

Because of the dispropotion between the azimuth and range resolution, the image is often *multilooked*, i.e. n azimuth pixels with the same range are averaged to form one. Now, the resolution is approximately same in both direction.

Let us also define that scene (image) *line* is a line of the pixels having the same azimuth coordinate, while the range coordinate changes. On the other hand, if we talk of a *pixel* coordinate, we mean the range direction pixel number.

For radar scenes, we need to recognize *slant range* and *ground range*. Taking the first pixel in a line as a reference, the ground range is the distance between the first pixel and the given pixel measured on the (flat) Earth surface, while the slant range is the difference between the distance measured to the first pixel and the given pixel from the satellite.

2.2 Steps of Interferometric Processing

Interferometric processing consists of the following steps:

- Image coregistration: A pixel in one image must accurately correspond to a pixel in the other image, i.e. one image must be shifted and resampled. The offset between the images is first computed from the known orbits, and then improved by computing the correlation of many small crops of the images. This is first performed coarsely, i.e. with the precision of few pixels, and then finely with small crops. To compute the offsets with accuracy of about 0.1 pixel, the images must be oversampled first. For image coregistration, image magnitude (terrain reflectivity) is used. The result of this steps are pairs of the corresponding pixels, i.e. shift vectors.

- Image filtering in the azimuth direction: This is performed between the coarse and fine coregistration, because the offset known from coarse coregistration (precise to the order of few pixels) is used. During filtering, the non-overlapping portions of the spectra are cut off (the scenes may have a different Doppler centroid value).

- Calculation of the coregistration parameters: The offsets obtained in various parts of the images with different reliability (correlation) are now approximated with a polynomial function (of a low order). After that, the residues must be computed and if they are large in an area, the polynomial function must be adjusted.

- Resampling of one of the images: After computing the coefficients of the polynomial function, the slave scene is resampled.

- Image filtering in the range direction: The spectra of the two scenes do not completely overlap in the range direction due to slightly different viewing angles of the two sensors (according to [14]). Range filtering should reduce the noise originating in this way.

- Interferogram creation: The phases of the two corresponding scenes are then pixel-wise subtracted (using complex conjugate multiplication):

$$I(i,j) = S_1(i,j) \cdot S_2(i,j)^* = |S_1|\,|S_2|\,e^{j(\varphi_1-\varphi_2)} \tag{2.2}$$

  where $I(i,j)$ is the interferogram value of the (i,j) pixel, $S_k(i,j)$ is the complex value of the master ($k=1$) or slave ($k=2$) scene (pixel (i,j)). Please note that j in the exponent denotes the imaginary unit.

- Computation and subtraction of the flat-Earth phase: The phase of the received signal (i.e. the difference between the received and transmitted signal) is largely

dependent on the distance between the transmitter/receiver and the reflector. We want the interferogram phase to be uniform if the imaged area has no topography. Before flat-Earth subtraction, the interferogram mostly consists of parallel lines in the azimuth direction; after subtraction, the most distinctive feature in the interferogram is topography.

- Coherence computation: Coherence is a measure for reliability of the phase in a small surrounding of a pixel (phase is a random value in a decorrelated area). Complex coherence is defined (according to [14]) as

$$\gamma_c = \frac{\mathcal{E}\left\{S_1 \cdot S_2^*\right\}}{\mathcal{E}\left\{S_1 \cdot S_1^*\right\} \cdot \mathcal{E}\left\{S_2 \cdot S_2^*\right\}} \tag{2.3}$$

  where the $\mathcal{E}$ operator is the mean value along a predefined area (e.g. 30 (original azimuth) by 6 (range) pixels). The real coherence is given by $\hat{\gamma} = |\gamma_c|$ and its value determines the quality of the interferogram in that area.

- Phase unwrapping: This is a critical step of the interferometric processing. The ambiguous phase in the $\langle -\pi, \pi)$ interval must be converted to an unambiguous value, which can be of any real value. The solution is ambiguous in principle, even if a point with a known phase is defined. This task is easy when the phase image contains no residues, i.e. wrapped phase differences in the small area of four neighboring pixels sum to 0 (more details can be found in [11]). For a more practical view, this condition is approximated by another two conditions:

  1. (true) phase differences between neighboring pixels do not exceed the value of π,
  2. the image does not contain noise.

  In practice, these conditions are rarely satisfied: even if the slopes are not too steep, the image is noisy in decorrelated areas (areas with vegetation and water surfaces). That is why phase unwrapping becomes an optimization problem and its solution depends largely on the interferogram itself and the method chosen. The most unreliable case for phase unwrapping is if a scene is divided by a continuous decorrelated area (e.g.a river) into two (or more) large areas with good coherence: then, these areas must be processed independently.

  More details about phase unwrapping can be found e.g. in [2, 3, 4, 11].

- DEM subtraction: In order to eliminate the topographic signal, an external DEM may be subtracted. This DEM needs to be radarcoded first (i.e. converted to the system of radar; after radarcoding it looks like an interferogram without noise and decorrelated areas) and then subtracted using a formula similar to (2.2). This is called the two-pass method.

- Differential interferogram creation: The other way to eliminate the topographic signal from an interferogram is to use an interferogram which is assumed not to contain deformation signal (for deformation mapping; this interferogram usually has a short temporal baseline). The topographical interferogram to be subtracted from

the other one must be first unwrapped and rewrapped to correspond with the other interferogram (the height ambiguity must be the same). Then, both interferograms are subtracted using a formula similar to (2.2). If both scene pairs (deformation and topographic) have a common master scene, the method is called three-pass interferometry.

- Phase filtering: Without filtering the phase, the interferogram looks very noisy. Local kernel filters are often used.

- Geocoding: transformation of the (line,pixel,phase) system of the interferogram to a geographic coordinate system (φ, λ, H_{el}). This can be performed using the satellite equations and the Doppler centroid of the scene, but this is usually not accurate enough. Also, at least approximate heights are required, especially in areas of high altitude or elevation changes. Please note that the interferogram phase contains only relative values and this is also the case of the heights; this error may be e.g. corrected by performing the geocoding twice.

  Also, tie points may be used for geocoding, but this approach is not implemented in DORIS software which we use.

2.3 Mathematical Model

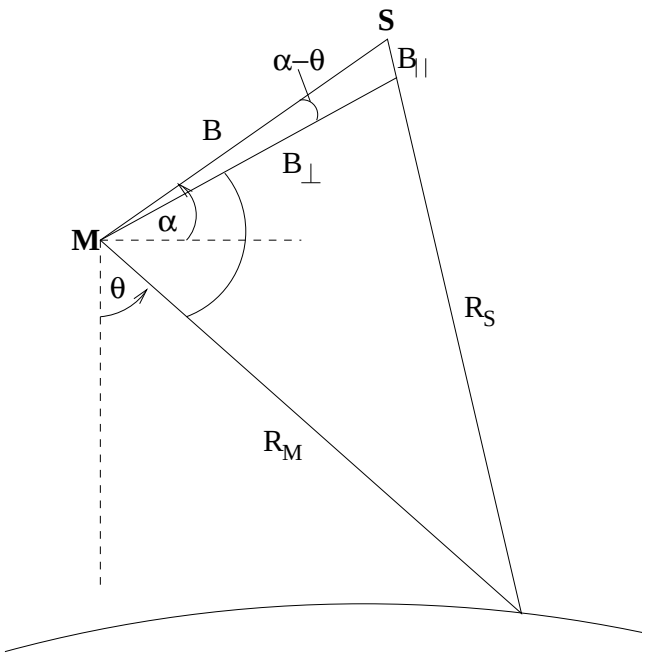

Figure 2.2: Mathematical model of radar interferometry, M denotes the satellite acquiring the master scene, S denotes the satellite acquiring the slave scene. This image was taken from [14].

The following derivation of the height ambiguity value and flat-Earth phase is taken from

[14]. The parallel and perpendicular components of baseline can be expressed as (see figure 2.2)

$$B_{\parallel} = R_M - R_S = B\sin(\Theta - \alpha), \tag{2.4}$$

$$B_{\perp} = B\cos(\Theta - \alpha). \tag{2.5}$$

Meaning of the symbols used should be clear from figure 2.2. Please note that we only deal with the plane containing both satellites and the reflector. The phases of a pixel corresponding to a reflector at the distance R_M from the satellite M and at the distance R_S from the satellite S are:

$$\Phi_M = -\frac{4\pi}{\lambda}R_M + \Phi_{errM}, \tag{2.6}$$

$$\Phi_S = -\frac{4\pi}{\lambda}R_S + \Phi_{errS} \tag{2.7}$$

where Φ_{errM}, resp. Φ_{errS} are phase errors due to e.g. atmospheric delay of the radar signal. The difference between the phases of the master and slave scenes (interferogram value) is therefore

$$\Delta\Phi = -\frac{4\pi}{\lambda}(R_M - R_S) + \Phi_{err} = -\frac{4\pi}{\lambda}B\sin(\Theta - \alpha) + \Phi_{err} = \Phi_E + \Phi_{tpg} + \Phi_{err} \tag{2.8}$$

where Φ_E is the flat-Earth phase

$$\Phi_E = -\frac{4\pi}{\lambda}B\sin(\Theta_0 - \alpha), \tag{2.9}$$

where Θ_0 is the look angle for the point on an arbitrary reference surface (this value changes according to the reference surface), Φ_{tpg} contains the topographic signal and Φ_{err} contains deformation and atmospheric signals.

According to formula (2.8), the topographic influence can be modeled as

$$\Phi_{tpg} = -\frac{4\pi}{\lambda}B\left(\sin(\Theta_0 + d\Theta - \alpha) - \sin(\Theta_0 - \alpha)\right) = -\frac{4\pi}{\lambda}B_{\perp}d\Theta, \tag{2.10}$$

where $\Theta = \Theta_0 + d\Theta$. Here we consider $d\Theta$ to be very small, i.e. $\sin d\Theta \approx d\Theta$ and $\cos d\Theta \approx 1$.

The height of a point on the Earth surface (above the reference surface) may be derived according to figure 2.3.

Assuming the interferogram contains only the topography signal, i.e. $\Phi = \Phi_{tpg}$, the value of $d\Theta$ is according to formula (2.10)

$$d\Theta = -\Phi\frac{\lambda}{4\pi}\frac{1}{B_{\perp}}, \tag{2.11}$$

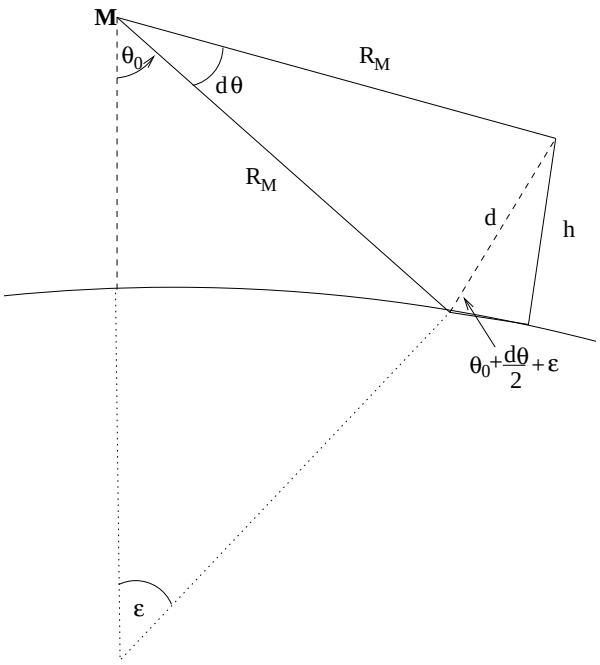

Figure 2.3: Height ambiguity derivation

the distance d is (see figure 2.3)

$$d = R_M\sqrt{2}\sqrt{1-\cos d\Theta} = 2R_M \sin\frac{d\Theta}{2}, \tag{2.12}$$

and the height h above the reference surface is therefore (see figure 2.3)

$$h = d\sin\left(\Theta_0 + \frac{d\Theta}{2} + \varepsilon\right). \tag{2.13}$$

By making a few substitutions we get (assuming $\sin^2\frac{d\Theta}{2} \approx 0$ and $\cos\frac{d\Theta}{2} \approx 1$)

$$h = 2R_M \sin\left(\Theta_0 + \varepsilon\right)\sin\frac{d\Theta}{2} \tag{2.14}$$

where $\Theta_0 + \varepsilon$ is the incidence angle.

The height ambiguity (i.e. the height difference corresponding to a 2π phase difference) is using (2.11) and (2.14) and considering $\sin\frac{d\Theta}{2} \approx \frac{d\Theta}{2}$

$$h_a = -R_M \sin\left(\Theta_0 + \varepsilon\right)\frac{\lambda}{2}\frac{1}{B_\perp}, \tag{2.15}$$

which is in accord with, e.g., [12]. However, this is only an approximate value, because R_M also changes with the look angle Θ. In addition, please note that the height ambiguity changes throughout the image: the length of the perpendicular baseline changes, and so

does the look angle Θ and the distance to the master satellite R_M. However, the height ambiguity is used for data selection and pair comparison, and it is precise enough for these applications.

For topography subtraction, we often use another interferogram (which we assume to contain only topographic signal). Let us call this interferogram a topo interferogram (and its phase Φ_{topo}) and the other one, which we intend to subtract topography from, a defo interferogram (its phase is Φ_{defo}). Also, let us suppose that both pairs have the same master scene (three-pass interferometry), therefore no resampling is neccessary. The topo interferogram must be unwrapped first and then rewrapped in order to have the same height ambiguity as the defo interferogram. Then, the phase may be subtracted.

More exactly, we can according to [14] start with defining the *deformation phase* $\Phi_{\Delta r}$, to correspond to the deformation occurred, Δ_r (and DEM differences and atmospheric signal, which can be neglected now)

$$\Phi_{\Delta_r} = -\Delta_r \frac{4\pi}{\lambda}. \tag{2.16}$$

and the phase of the deformation interferogram can be written as

$$\Phi_{defo} = \Phi_{topo} \frac{B_{\parallel defo}}{B_{\parallel topo}} + \frac{4\pi}{\lambda}\Delta_r, \tag{2.17}$$

but the "true" parallel baselines are unknown.

On the other hand, according to [14], the phase of the defo interferogram may be written as (using formula (2.10))

$$\Phi_{defo} = -\frac{4\pi}{\lambda} d\Theta B_{\perp defo} - \frac{4\pi}{\lambda}\Delta_r \tag{2.18}$$

and the phase of the topographic interferogram is expressed by formula (2.10), except that we would write $B_{\perp topo}$ instead of $B_\perp$. (Please distinguish the index $_{tpg}$, denoting only the topographic component of the phase, and the index $_{topo}$, denoting the phase of the particular interferogram.) Therefore, the phase of the deformation interferogram (after subtracting the topographic phase) is

$$\Phi_{\Delta_r} = \Phi_{defo} - \frac{B_{\perp defo}}{B_{\perp topo}} \Phi_{topo}. \tag{2.19}$$

In other words, the phase of the differential interferogram depends on the baselines of both pairs. And because both baselines change a little throughout the image, the phase of the differential interferogram may change, too.

2.4 Applications and requirements

The interferogram (after flat-Earth phase subtraction) contains the following signals:

- topographic signal: corresponds to the actual height of the ground spot (reflector),

- deformation signal: corresponds to the deformations occurred between the acquisition of the two scenes,
- atmospheric signal: corresponds to the delay of the signal caused by its pass through the atmosphere,
- orbit errors influence: the phase changes due to the imprecise satellite positions,
- DEM errors: the difference between the real topography in the moment of acquisition and the available DEM to be subtracted; when using the two-pass method, also the error of the coregistration between the interferogram and the DEM must be considered.

Interferometry is often used for DEM creation. In this case, the perpendicular baseline should be as large as possible, in order to reach a low height ambiguity and therefore a high height accuracy of the DEM. The upper limit of the spatial baseline is about 2 km; for such a long spatial baseline, the two scenes may be too different to allow coregistration. On the other hand, the temporal baseline should be as short as possible in order not to allow too much decorrelation and deformations.

When used for deformation mapping, the perpendicular baseline should be as short as possible in order to reduce the topographic signal in the interferogram as much as possible. Even if the interferogram contains the topographic signal and a DEM must be used in order to eliminate it, a higher height ambiguity means worse accuracy requirements for the DEM. The temporal baseline should be long enough to allow the deformations to occur, but the deformations can't be too large. (If the deformation slope exceeds 2.8 cm/px, phase unwrapping is very irreliable, and large deformations also cause decorrelation, especially when occuring in the azimuth direction.) An optimal way is to process a larger set of scenes. There are many "spots" in an interferogram which need to be verified in other interferograms or by other method in order to be sure they are caused by deformation.

Foreign research groups often map deformations after an earthquake; these earthquakes often occur in a desert, so there are no decorrelated areas there and the deformations are large enough to produce fringes. Detecting landslides is more difficult, because the landslides themselves often cause decorrelations and may not be large enough to be visible in an interferogram.

It is also possible to determine some properties of the atmosphere using radar interferometry. It has been proven (see e.g. [29, 30]) that weather changes (fronts, storms) cause a great heterogeneity in the signal delay.

For topographic or deformation mapping, data selection is often performed with the purpose to eliminate these effects, i.e. no rain and snow dates are preferred. If there is no storm (or similar phenomenon) in the mapped area, the atmospheric influence usually has a "long-wave" characteristics, i.e. changes slowly in the area (see e.g. [12]).

The atmospheric influence (i.e. delay) depends not only on the weather conditions, but, according to [13], it also depends considerably on the range, i.e. on the look angle. For an increasing look angle, the path of the ray through the atmosphere gets longer. The

atmospheric delay may reach the value of 15 m but the difference between the two acquisition should be lower. This influence is significant in the case of very short perpendicular baseline and one acquisition performed at night and the other during the day which is never the case for scenes acquired by the same satellite and at the same track.

Also, the atmospheric delay depends strongly on topography, which should not be significant in our lowland area of interest.

Let us emphasize here that the orbit errors and atmospheric influences cannot be recognized from each other: they both mostly have a long-wave character (see [12]). They should be reduced together, establishing *fictive satellite positions* which are *obtained by minimizing the number of residual fringes in the interferogram. If we use fictive satellite positions, artifacts are corrected at the four corners of the image so the worst artifact occurs close to the center of the image* [29].

However, the atmospheric delay influence is independent of the height ambiguity and according to e.g. [12], it can exceed several fringes. That means that the error of the extracted DEM could be quite large and can be determined (or eliminated) using equally distributed tie points. On the other hand, for our application, these errors are not very significant — we are only interested in the trend of the atmospheric delay within the scene.

Another important feature of the method is that all measurements are relative. Theoretically, the phase of the differential interferogram should be zero in the areas of no deformation, but there are systematic errors influencing the measurements and therefore the deformations (or DEM) can be determined only relatively with respect to the surroundings.

2.5 Problems of the Method

The most important problem of the method is decorrelation. All vegetated areas are decorrelated due to the fact that their surface changes (the movement of leaves etc.) are comparable to the radar wavelength. The only possibility is to acquire both scenes simultaneously, such as in the SRTM mission.

Water surfaces are always decorrelated. The surface moves so quickly that it is impossible to see it correlated even in the case of simultaneous acquisition of both scenes.

In our area of interest, which is full of open mines, another problem may be "DEM errors", i.e. an old DEM. Also, DEMs from different sources may cause a problem because radar interferometry (C-band) maps the top of a forest, in comparison to geodetic methods, which map the ground.

For the case of two-pass interferometry, where an external DEM is used for topography subtraction, one more problem arises: coregistration of the DEM to the radar system; in DORIS, the (radarcoded) DEM can only be shifted by an integral number of pixels (in both directions). I think that this is quite a limitation of the software and may cause errors, especially in mountainous areas. In addition, the shift can only be figured out manually or by trial-and-error procedure.

A little disadvantage of the two-pass method with the use of SRTM DEM is that DORIS works in the WGS-84 coordinate system and the heights are related to the WGS-84 ellipsoid, while the SRTM DEM is related to the geoid. Fortunately, the difference between the bodies is neglectable in the areas where the geoid-to-ellipsoid offset is changing only slowly (i.e. causes only a bias).

Chapter 3

Satellites and Orbit Accuracy

In order to be usable for SAR interferometry, a satellite must have following features:

- it must carry a synthetic aperture radar (SAR) onboard,
- the satellite's position must be recorded in the moment of the acquisition of a scene.

For DEM generation, scene pairs with the shortest possible temporal baseline are used. An ideal case for this application is the tandem mode of the ERS-1 and ERS-2 satellites, one following the other in 24 hours. On the other hand, scene pairs with a longer temporal baseline (the actual desired temporal baseline depends on the deformation type) are used for deformation mapping, and scene pairs from the same satellite are often used here.

For interferometry, the following satellites may be used (more details can be found in [25]):

- ERS-1 (C-band), launched by European Space Agency (ESA) in 1991, deactivated in 2000,
- ERS-2 (C-band, the same frequency as ERS-1), launched by ESA in 1995, still active,
- RADARSAT (C-band), launched by Canadian Space Agency in 1995, still active,
- JERS-1 (L-band), launched by Japan Aerospace Exploration Agency in 1992, deactivated in 1998,
- JERS-2 (L-band), launched by NASDA (now JAXA) in 1999, still active,
- ENVISAT (C-band), launched by ESA in 2002, still active.

Combination of scenes from different satellites (if they are operating on different orbits) is complicated due to a different incidence angle, often even impossible. It is possible to combine scenes acquired by ERS-1/2 with scenes acquired by ENVISAT although the radar wavelength is slightly different, but there are requirements with respect to the baseline

length, and coherence behaviour is far different in comparison to conventional interferometry [10, 1]. On the other hand, it is possible to combine the generated interferograms.

Also, it is discouraged to use data from different tracks of the satellites (see [18]) due to the largely different incidence angle causing different scattering effects influencing both the signal magnitude and phase.

In our project, we use only the ERS-1/2 scenes acquired in 1998/1999; we also aim to use ENVISAT scenes in the future.

3.1 Satellite Equipment

This section deals with satellite instruments used for satellite positioning. The only satellites of our interest are ERS-1/2 and ENVISAT because we do not use and do not plan to use data from any other satellites. We will omit instruments used for other purposes than those which are able to improve/verify satellite position information.

The principles of the systems will be described in section 3.3.

3.1.1 ERS-1/2

All satellite instruments on ERS-1/2 are listed e.g. in [23]; we will only provide the description of the instruments used for satellite position measurements. ERS satellites have (according to [23]) the following instruments onboard:

- (nadir) radar altimeter — measures the height of the satellite above the terrain (broke down at ERS-1 in June 1996),
- microwave sounder — measures the water vapour content in the atmosphere, the measured data are used for radar altimeter measurements corrections,
- precise range and range-rate equipment (PRARE) — a satellite positioning system, which evaluates the position and velocity of the satellites with respect to up to 4 transponders on the Earth. Unfortunately, the PRARE system on ERS-1 failed soon after the launch [23],
- laser retro-reflector (LRR) — a reflector on the satellite which reflects laser rays transmitted from Earth stations. For ERS-1, this instrument provided the only way to compute its precise orbits for a long time.

3.1.2 ENVISAT

All the instruments onboard ENVISAT are listed e.g. in [7], for satellite positioning the following ones may be used:

- (nadir) radar altimeter 2 — an enhanced radar altimeter, the precision of the delay determination is less than a nanosecond,

- microwave radiometer (MWR) — used for radar altimeter measurements corrections (similar to the microwave sounder),
- Doppler orbitography and radiopositioning integrated by satellite (DORIS) — provides velocity measurements utilizing stations on the Earth. The data are used for precise orbits computations with an accuracy of the order of centimeters,
- laser retro-reflector (LRR) — a reflector on the satellite which reflects laser rays transmitted from Earth stations.

3.2 Satellite Behaviour and Phases

In this section, basic information about satellite phases of operation for ERS-1/2 and ENVISAT is given. It also deals with the satellite instruments availability. ERS-1 operated in various modes during its life and the data availability and quality depended on it.

3.2.1 ERS-1/2

ERS-1 and ERS-2 are not exactly twins, with ERS-2 carrying one more instrument and at the time of launch weighing almost 200 kg more than ERS-1. Their altitude is about 780 km, and they are orbiting in nearly circular and sun-synchronous trajectory with 98.5 ° inclination. The satellite cycle is 100 minutes long and in 35 days (ERS-1 only in some phases), the satellite returns back to the same track; therefore, in 35 days, the same area is imaged again (the total number of tracks is 501). A given place on the Earth is imaged approximately every three days.

The start and stop dates of the particular phases of the ERS-1 satellite are shown in table 3.1 and are taken from [9, 20, 24]. ERS-2 is in a multi-disciplionary phase all the time (with repeat cycle of 35 days).

Phase	Start date	Stop date	Repeat cycle
Commissioning Phase	July 25^{th}, 1991	December 10^{th}, 1991	3 days
Ice Phase	December 28^{th}, 1991	March 30^{th}, 1992	3 days
Roll Tilt Mode	April 4^{th}, 1992	April 13^{th}, 1992	3 days
Multidisciplinary Phase	April 14^{th}, 1992	December 21^{st}, 1993	35 days
Second Ice Phase	December 23^{rd}, 1993	April 10^{th}, 1994	3 days
First Geodetic Phase	April 10^{th}, 1994	September 28^{th}, 1994	168 days
Second Geodetic Phase	September 28^{th}, 1994	March 21^{st}, 1995	168 days
Tandem Phase	March 21^{st}, 1995	June 5^{th}, 1996	35 days
Hibernation (back-up)	July 1996	July 1998	35 days
Multidisciplionary phase	July 1998	March 2000	35 days

Table 3.1: Start and stop dates of the particular ERS-1 phases.

Phase description

During the Ice phases, ERS-1 was intended to map Arctic ice coverage with higher frequency, therefore the repeat period is shortened and some tracks are not visited at all.

During the Roll Tilt phase, the SAR acquired data with different look angle (35 °). The satellite had to rotate and the performance of the radar altimeter may have been degraded, worsening the orbit determination quality.

The 35-day cycle (during the multidisciplinary and tandem phases) has the following advantages over the 3-day cycle: the entire Earth is covered with SAR images and the ground altimeter tracks are only 39 km apart (at 60 ° latitude), which implies denser tracks and therefore more chances to adjust the Earth gravity model.

The repeat period of the satellite is heavily influenced by the semi-major axis of the satellite. Even a small change in the value of the semi-major axis may cause a large change in the repeat period. The semi-major axis is naturally getting shorter but it can be changed during a satellite maneuvre.

The first and second geodetic phases have the same features, except that the track of the second one is shifted in comparison to the first one. The purpose of these phases is to improve the Earth gravity model using the radar altimeter. SAR operates normally in these phases, except for the fact that the scenes are shifted a bit with respect to each other. In addition, SAR scans a different location each time, therefore the combination of the scenes into iterferometric pairs may be limited due to decorrelation caused by different incidence angles of the scenes (large perpendicular baseline).

In the tandem phase, both satellites are in the same orbit, ERS-2 following ERS-1 with 24-hour delay. This allows acquisition of the scenes from the same orbit (two scenes from different orbits are impossible to process in SAR interferometry), with such a short temporal baseline that almost no deformations had time to occur, atmospheric delay changed a little and these scenes are better correlated than the pairs with longer temporal baseline, too. Also, the tandem phase was a unique occasion to improve the knowledge about the Earth gravity field (will be described in section 3.5).

During the hibernation phase, the system was woken up every 70 days for three days, allowing to test the system state. However, the satellite has not been tracked by satellite laser ranging (described in section 3.3) [20].

Limitations and failures

In June 1996, the altimeter on ERS-1 stopped working, and the orbits from satellite laser ranging are not accurate enough (only "fast-delivery" orbits are available since that time).

The PRARE system onboard ERS-2 began operating in January 1996.

Data recording system on ERS-2 run out of its capacity in June 2003, therefore after that, data could only be acquired in the case when a ground station is in a line of sight.

In January 2001, ERS-2 had a problem with gyroscopes and was yawed in comparison to its correct position. During January 2001, the ERS-2 did not acquire SAR data, but starting from February 6, when it got back to its orbit, it again started acquiring scenes.

However, the satellite was yawed and the data had a large value of Doppler centroid until February 2003, when a new ground station able to compensate for the satellite yaw was built. Since that time, the data can again be formed into interferometric pairs almost without limitations.

Usability for SAR interferometry

For SAR interferometry, the data acquired during the Tandem phase are mostly used. The advantage of it is that the temporal baseline is only 1 day, allowing to create DEM with quite good coherence.

The disadvantage of the Ice phases is that not the entire area was covered; on the other hand, the temporal baseline was short enough to provide better coherence.

The disadvantage of the Geodetic phases is that data of the same area are shifted (in range) and the coherence may be worse due to a different incidence angle.

Data acquired during the Roll Tilt phase should not be used at all due to a different look angle (especially combinations of data from Roll Tilt phase with other data) and worse performance of radar altimeter, worsening the precision of the precise orbits.

3.2.2 ENVISAT

The ASAR onboard ENVISAT allows operation in 37 modes (different polarisation, different look angle and different resolution) but it operates in some modes only upon a requirement.

The ASAR has a different frequency than the SARs on ERS-1/2, which is 5.331 GHz (i.e. the difference is 31 MHz).

The repeat cycle is 35 days, same as for ERS-1/2, the altitude and incidence angle are also the same. The only feature to change is the local solar time of the pass of the satellite above the equator, which is adjusted by half an hour.

But, the ESA catalogue only offers two scenes of the northern Bohemia acquired during ENVISAT operation. Therefore, at the time being it is impossible to perform interferometric processing of this data: only one interferometric pair is insufficient. We hope that data availability will get better in the future.

3.3 Satellite Tracking Systems and Their Accuracy

In this section, systems for finding the satellite position are described. They are based on measuring the distance between a place on the Earth surface and the satellite, eventually also the radial speed. By combination of more ground stations, all the components of the position may be obtained.

3.3.1 SLR

SLR (Satellite Laser Ranging) means measuring the round-trip distance between the corner reflectors (LRR) on the satellite and ground stations. A laser emits a high-power short pulse and waits for the reflection (the position of the satellite is approximately known). The laser cannot penetrate clouds, so the measurements are weather-dependent.

The measured distance must be corrected for the distance between the LRR and the satellite gravity center, tropospheric delay, atmosperic refraction and satellite aberation.

Some stations observe the distances with less accuracy than others; these observations must therefore be downweighted when processing all the observations altogether. The accuracy of one observation ranges from 1 cm to 20 cm [19], depending largely on the accuracy of the corrections performed.

There are about 80 to 200 SLR observations to be processed daily [19]. There are 24 stations all over the world, 10 of them in Europe. Unfortunately, these 10 station perform about 57 % of the observations; there are only 3 stations in the southern hemisphere, performing only 13 % of the observations (the worst case happened in 1992, see [19]).

The problem of this method in comparison to other methods is that the observations are performed manually, the ground network is scarce and not well-distributed, and that there may be large gaps betweeen the observations (the longest delay between successive ERS-1 observations was almost 30 hours). Therefore, the accuracy of the processed orbits varies a lot. If the observation conditions are good, the accuracy is a few centimeters (i.e. comparable to other methods).

More details about SLR may be found in [19].

3.3.2 PRARE, DORIS

Both PRARE and DORIS systems are based on measurements of the Doppler shift of the received (microwave) signal, i.e. both systems are weather-independent (except for different atmospheric delay). PRARE is an acronym for Precise Range And Range-rate Equipment, DORIS is an acronym for Doppler Orbitography and Radiopositioning Integrated by Satellite. The radial speed of a satellite with respect to a ground station is obtained by applying the Doppler principle, i.e. that the frequency of the received signal is different from the frequency of the transmitted signal.

In addition to speed measurements, both systems also serve for positioning. This is obtained by measuring the round-trip time of the signal and also by integrating the velocity.

There are many stations on the Earth that measure the radial speed of the satellite: consequently, we can obtain the complete velocity and position vectors in consequence. The network of stations is better than that for SLR for both systems; however, the network is better distributed for the DORIS system than for PRARE.

The measured distances need to be corrected for tropospheric and ionospheric delays, and also for satellite aberation.

All measurements need to be corrected for the distance between the reference point of the antenna and the satellite gravity center.

The behaviour of both systems is discussed below.

PRARE

Two continuous signals are transmitted from the satellite to the Earth, one of them is in X-band, the other in C-band, which allows to correct for ionospheric influence. In addition to the code, neccessary for distance measurements (similar to GPS), an information is transmitted.

The time of reception of the two (simultaneously transmitted) signals is recorded at the ground stations and the processed data are transmitted back to the satellite, as well as certain meteorologic informations of the station. The ionospheric corrections are applied later during the processing which is performed on the satellite.

The precision of the PRARE system is about 0.1 mm/s in the velocity and 2.5–6.5 cm in the position (both are root squared sums) [8].

More details about the PRARE system may be found in [8].

DORIS

The precision in the radial velocity is about 0.4 mm/s, giving better precision of the orbits than 5 cm in altitude [7].

The signal is transmitted from a ground station and received by the satellite where it is processed, giving the almost real-time orbits.

Similar to the PRARE system, DORIS operates at two frequencies, one for precise measuring (above 2 GHz), the other for evaluation of the ionospheric correction (about 400 MHz).

More details about the DORIS system may be found e.g. in [6].

3.3.3 Radar Altimeter

Radar altimeter measures the distance between the satellite and the Earth surface: not only oceans, but also continents and glaciers. However, the altimetric data of vegetated or built-up areas are useless. Both transmitter and receiver are on the satellite and the Earth surface serves as a reflector. It is often used for other purposes: Earth gravity model determination, ice coverage research, oceanographic applications etc.

Only nadir altimeter can be used for orbit determination — the antenna must be oriented towards the Earth center.

For orbit determination, the radar altimetry data are used only at the ocean tracks.

The altimeter measurements are subject to the following corrections (see e.g. [16]):

- the distance between the reference point of the antenna and satellite gravity center,

- atmospheric delay — both ionospheric (may be eliminated if the measurements are performed using different frequencies) and tropospheric (computed with use of an atmospheric model),
- tidal influence,
- geoid-to-ellipsoid offset,
- sea-surface topography (having a constant and a variable component).

The footprint of the ERS-1/2 and ENVISAT satellites is about 1.7 km wide, and the effective width of the pulses is about 3 ns (the pulse of length 20 ms is linear frequency-modulated) [7].

The resolution of the altimeter is about half a meter (in the vertical direction), but it is about one order of magnitude better over oceans (the sampled reflected signal is fitted with a model function). The highest accuracy (according to [7]) is 4.5 cm.

Similar to DORIS and PRARE systems, RA-2 altimeter on ENVISAT operates at two frequencies (Ku-band and S-band), allowing to correct for ionospheric influence, which is frequency dependent. The altimeter on ERS-1/2 operates at a single frequency.

Two ways of using altimeter data

The fundamental equation of (conventional) satellite altimetry has the form of

$$r = h + SST(v) + STT(p) + T + N + r_e, \tag{3.1}$$

where r is the distance between the Earth center and the satellite, h is the altimeter-measured distance (corrected for the ionospheric and tropospheric delays and for the additive system error), $SST(v)$ is the variable component of the sea-surface topography, $SST(p)$ is the constant component of the sea-surface topography, T is the tidal influence, N is the ellipsoid-to-geoid offset and r_e is the ellipsoid radius in the respective point.

Conventional altimetry processes the measured heights corrected for the noticed influences and may study the ocean currents or ellipsoid-to-geoid offset etc. Cross-over altimetry evaluates the differences between the measurements in the ascending and descending tracks in one place, serving to determine Earth-gravity model or variations in sea-surface topography.

For cross-over altimetry, we may use either data from one satellite, or data from two satellites and evaluate the cross-over differences between

- the ascending track of the first satellite and the ascending track of the other satellite, and
- the descending track of the first satellite and the ascending track of the other satellite, and
- the ascending track of the first satellite and the descending track of the other satellite, and

- the descending track of the first satellite and the descending track of the other satellite.

The fundamental equation of cross-over altimetry has the form of

$$r_a - r_d = h_a - h_d + SST(v_a) - SST(v_d) + T_a - T_d, \tag{3.2}$$

where index a denotes the ascending track and index d denotes the descending track. The other terms of formula (3.1) were eliminated by subtraction. Of course, the equation (3.2) applies for the cross-overs of the ascending and descending tracks and cannot be used for geoid determination and measuring the constant component of the sea-surface topography.

The cross-over differences (XDs), as given by (3.2), are a measure of precision of the radial orbit perturbation. Altimeter data can also be an instrument for orbit determination; however, all the influences described in (3.1) must be modeled first.

The cross-over altimeter data are often considered to be independent on the conventional altimeter data, if used for orbit determination or Earth gravity model improvement.

The altimeter data can be used for two purposes (of our interest):

- orbit determination – conventional altimetry,
- gravity field improving – both conventional and cross-over altimetry.

3.4 Orbit Error Characteristics

The orbit may be errorneous in three directions:

- *along-track error* ("timing" error), i.e. the satellite is on the same track as it should be, but somewhere else: these errors are not necessary to deal with in radar interferometry [12] because they are approximately perpendicular to the baseline. However, the orbit is the least accurate in this direction,
- *radial error*, i.e. the nadir distance from the satellite to the Earth (i.e. the distance measured by a nadir altimeter) is errorneous,
- *across-track error* which is perpendicular to both of the previously defined components.

Due to the principles of satellite positioning methods (will be described in section 3.5), the radial RMS error is the smallest. For DEOS precise orbits, the radial error is said to be in the order of 5–6 cm, and the across-track error in the order of 15 cm [20].

3.5 Precise Orbit Determination and Its Accuracy

This section is based on [20, 26, 27].

Precise orbits, unlike predicted or fast-delivery orbits, are available several months later. In interferometry, this is typically not an obstacle, the data are usually processed long time after their acquisition. But on the other hand, precision of the orbits is required in order for the image coregistration to be performed reliably.

The orbits are delivered as a part of the satellite data. However, these are predicted orbits and their precision is not better than 25 m [5]. For interferometric purposes, precise satellite orbits are needed.

Precise orbits are obtained by combination of various methods described in the previous section. However, these instruments do not measure the satellite position all the time and the position must be interpolated. Therefore, a precise Earth gravity model and a satellite geometry model need to be used.

The precise orbits are given for arcs about 5.5 days long, 3.5 days apart from each other (thus, there is a 2 day overlap between the arcs). The orbits are given in CTRS, with mean IERS pole, altitude is given above the GRS-80 ellipsoid.

There are two basic sources of precise orbits of ERS-1/2 satellites: ESA itself and DEOS (Department of Earth Observation and Space systems at TU Delft). The radial error of the ESA precise orbits is estimated at 8–10 cm, the radial error of the DEOS precise orbits is estimated at 5–6 cm [5]. The difference between them is caused by different models of Earth gravity field and satellite geometry used.

We use only the DEOS precise orbits, so this section will deal only with these.

After the failure of ERS-1 altimeter, the orbits are no longer precise, they only have the status of fast-delivery orbits which are not so accurate (computed only from SLR data).

The precision of fast-delivery orbits is a little worse than that of precise orbits; during the ERS-2 mission, the difference was only 2 cm in the radial direction and about 8 cm in the along-track and cross-track directions. This precision is worsened if the satellite has performed a manoeuvre recently.

3.5.1 Orbit determination

The forces which influence satellite movement can be divided into two categories:

- *conservative forces*, i.e. the gravitational influence of the Earth (including tides), Moon, Sun and other planets (mostly negligible). To model these, a precise model of the gravity of the Earth and other bodies is required. These forces influence the orbit at most;
- *non-conservative forces*, of which the most significant are atmospheric drag and solar radiation pressure. To model these, a precise satellite geometry model (including orientation) is required. On the other hand, a satellite may contain an instrument to correct for these in order for the satellite not to be influenced by these forces. However, this is case of neither ERS-1/2, nor ENVISAT.

The orbit determination for ERS-1 is difficult with the absence of PRARE. SLR data, as described in section 3.3, are not well distributed in the orbit and the orbits obtained from them contain therefore large errors, especially above the southern hemisphere. However, the SLR data, together with altimeter data, are used for ERS-1 orbit determination.

In 1991, the radial orbit error of ERS-1 was more than a meter, caused by an imprecise gravity model and inappropriate model of satellite geometry. In 1998, the radial orbit error of ERS-1 was only about 5 cm. In addition to the improvement of the two models, this was caused by including the cross-over altimetry data into the precise orbit determination procedure [26].

Delft Institute for Earth-oriented Space Research (DEOS) tailored Earth gravity model DGM-E04 (Delft gravity model) in order to cut down the radial orbit error. This model emanates from the JGM-3 gravity field model. For its construction, single satellite cross-over data were used, and during the tandem mission, also the dual-satellite cross-over data between ERS-1 and ERS-2. The model should be the best for satellites on the same orbit as ERS-1/2, i.e. also for ENVISAT. For testing the model, conventional altimeter data and ERS/Topex dual satellite cross-overs remain.

Before processing the cross-over altimeter data, the following are omitted:

- if the angle between the ascending and descending track is shallow, or
- if the time interval between the acquisitions is larger than 17.5 days, which is half of the repeat period of ERS-1/2, or
- if there is an insufficient number of measurements near the cross-over point.

The weight of the radar measurement differs in dependence on geographic location and sea-surface variability, which is known from previous processing of altimeter data.

3.5.2 Gravity model tailoring

For gravity model tailoring, altimeter data from ERS-1/2 are used. The tandem phase was most important, allowing to create a large amount of dual-satellite cross-overs to take into account.

The process of Earth gravity model tailoring has two steps:

- first, the gravity-induced orbit error must be isolated from the error caused by inappropriate satellite geometry modelling. The influence of gravity is different from the influence of non-conservative forces;
- second, the gravity model parameters (Stokes's coefficients) are adjusted in order to minimize the error.

Lagrange's planetary equations allow to compute the time-derivatives of each Keplerian element in dependence on the other Keplerian elements and the gravity perturbations. The consequence of the equations are described below; for more details, see [17].

According to [17], the following Keplerian elements change (linearly) secularly due to gravity perturbations:

- the longitude of the ascending node Ω,
- the argument of perigee ω, and
- mean anomaly M.

Gravity does not cause the other three Keplerian elements (the semi-major axis a, eccentricity e and inclination i) to change secularly.

The secular changes of these are included in orbit computations, other influences are considered to be orbital perturbations.

The atmospheric drag has a neglectable influence for ERS-1/2 due to the high satellite altitude, while the solar radiation pressure causes pseudo-secular changes of all Keplerian elements.

Radial orbit perturbation

The distance between the Earth center of gravity and the satellite r is

$$r = a\left(1 - e\cos E\right), \tag{3.3}$$

where a is the semimajor axis, e is the eccentricity and E is the eccentric anomaly and the relationship between the eccentric and mean anomaly M (which is a Keplerian element) is

$$M = E - e\sin E. \tag{3.4}$$

Radial orbit perturbation is then expressed as a function of the perturbations in Keplerian parameters [22]

$$\Delta r = \frac{\partial r}{\partial a}\Delta a + \frac{\partial r}{\partial e}\Delta e + \frac{\partial r}{\partial M}\Delta M, \tag{3.5}$$

where Δ is a symbol for perturbation.

The perturbations in Keplerian elements are computed from the Lagrange's planetary equations with use of Stokes's coefficients of various degrees and orders; some of them are more significant than others, depending on the orbital parameters, above all the semi-major axis a, eccentricity e, and inclination i.

As a result, the perturbation Δr can be expressed as a five-order series, with the parameters of l, m (degree and order of Stokes's coefficients), p, q (summing coefficients, $0 \leq p \leq l$, $-\infty < q < \infty$) and s, the order of Bessel functions used for approximating equation (3.3). The expression can be simplified to [26]

$$\Delta r = \sum_{l=1}^{\infty}\sum_{m=0}^{l} \Delta r_{lm}^{c} \pm \Delta r_{lm}^{s} \tag{3.6}$$

with

$$\Delta r^c_{lm} = Q^c_{lm} \left(\Delta C_{lm} \cos m\lambda + \Delta S_{lm} \sin m\lambda \right), \tag{3.7}$$
$$\Delta r^s_{lm} = Q^s_{lm} \left(\Delta C_{lm} \sin m\lambda - \Delta S_{lm} \cos m\lambda \right), \tag{3.8}$$

where Q^c_{lm} and Q^s_{lm} are functions of latitude only and further depend on Keplerian parameters a, e, i [26].

As a result, gravity-induced radial orbit perturbations are partially geographically correlated (the perturbation depends not only on the geographical location but also on the direction of the overpass). That means that part of the perturbation has the same value for both ascending and descending passes. However, the gravity influence is the same for all passes of the same direction above a given area.

Papers [22, 26] consider which gravitational coefficients influence the cross-over differences (XDs). These gravitational coefficients can therefore be adjusted with the knowledge of cross-over differences, and the value of the XDs is cut down. The other parameters, such as the zonal coefficients ($m = 0$), of the gravity models can be adjusted with the help of satellites on different orbits or by other methods.

DGM-E04 gravity model, which was tailored from the ERS-1/2 altimeter data, was at first verified in SPOT-2 (has an orbit similar to ERS-1/2) orbit determination application. The data were compared to DORIS data.

Only 30 % of the ERS-1/2 tandem mission data were used for DGM-E04 tailoring, the rest was used for its verification.

However, this gravity model should be the optimal for ERS-1/2 and all satellites on the same or similar orbit.

Orbit accuracy estimation

Precise orbits were compared with SLR data. This allowed measuring of the accuracy in all directions (not only the radial accuracy). Please note that SLR data have not been used for DGM-E04 tailoring. In addition to SLR data, cross-over differences were used for orbit accuracy estimation (only in radial direction).

RMS of SLR residuals is 4.9 cm for DGM-E04, while RMS of XD residuals is 8.1 cm, approximately equal for ERS-1 and ERS-2 [26]. However, a systematic range bias and time tag bias can be isolated from altimeter measurements, pressing the residual RMS down.

The RMS of residuals of ERS-1/Topex cross-over differences is only 3.3 cm, measuring the accuracy of determinating the geographically fully correlated radial perturbation of ERS-1 (Topex orbits are considered to be much more accurate than those of ERS-1) [26].

Chapter 4

Orbit Inaccuracy Influence

First, let us recognize two ways how an orbit error can influence the interferogram:

- the scene is shifted with respect to both reality and the other processed scene; therefore, the shift computed from orbit parameters is different from the shift computed by magnitude image correlation;
- the perpendicular baseline has a wrong value, causing the interferogram to be sloped; in addition, the wrong value of perpendicular baseline causes a wrong value of height ambiguity needed for phase-to-height conversion.

In this chapter, we will not consider the scene shift influence, this will be considered later. This chapter deals with the influence of wrong baseline parameters on the interferogram.

Therefore, let us transfer the problem to the plane containing both satellites and the imaged place on the Earth. This plane is approximately perpendicular to the satellite tracks; the tracks are considered to be approximately parallel.

The along-track error (timing error), i.e. the satellite is on the same track as it should be but somewhere else (after coregistration, this error should not be larger than approx. one tenth of a pixel, i.e. half a meter) only slopes this plane but the baseline is not changed significantly. The along-track error may only cause a problem for a very short baseline; however, we did not meet such a case (for baseline length $B = 16$ m and along-track error of 0.5 m, the baseline is lengthened by 8 mm.

We will therefore need only a two-dimensional orbit error, considering in accord with [12] only the radial and across-track components.

In addition, the absolute orbit errors are not as important as the relative ones, i.e. the baseline errors. That means that an inaccurate Earth gravity model does not influence the interferogram as much as an imprecise satellite geometry model, causing the atmosperic drag and solar radiation pressure influences to be incorrectly modeled. The reason for this is that the satellite is approximately at the same position at the moments of both acquisitions.

Baseline representation

For baseline inaccuracy influence, we will consider a different baseline representation than before, illustrated in figure 4.1. Horizontal and vertical components are the same for all pixels in a single line in the interferogram (in contrast to the parallel and perpendicular components) and they allow us to consider different accuracy of the radial and across-track component. Let us note here that the following text only considers the plane defined by the two satellites and the imaged place on the Earth.

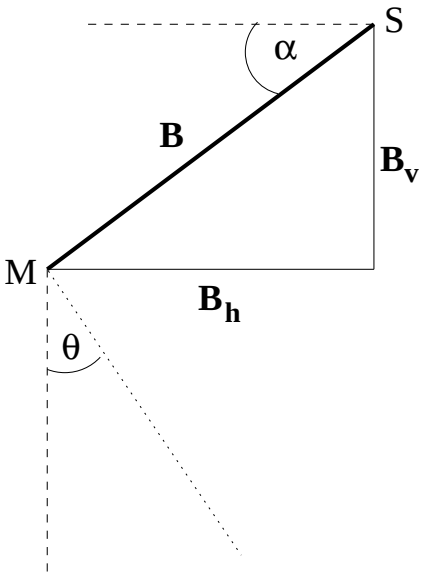

Figure 4.1: Baseline representation

The formulas for transformation between various baseline representations (parallel – perpendicular, horizontal – vertical and baseline legth – baseline orientation) may be found e.g. in [12]:

$$B_h = B\cos\alpha = B_\perp\cos\Theta + B_\parallel\sin\Theta, \tag{4.1}$$
$$B_v = B\sin\alpha = B_\perp\sin\Theta - B_\parallel\cos\Theta, \tag{4.2}$$
$$\alpha = \arctan\frac{B_v}{B_h}, \tag{4.3}$$
$$B = \sqrt{B_h^2 + B_v^2}, \tag{4.4}$$
$$B_\perp = B_h\cos\Theta + B_v\sin\Theta, \tag{4.5}$$
$$B_\parallel = B_h\sin\Theta - B_v\cos\Theta. \tag{4.6}$$

Let us stress here that the sign of the perpendicular baseline is also important for understanding the influence and let us define the sign in accord with [12]: $B_\perp$ *is positive whenever satellite S is located to the right of the slant range of satellite M.*

Three errorneous values, which can influence the interferogram, are considered:

- horizontal baseline B_h,
- vertical baseline B_v,
- and radar wavelength λ.

All three of them cause the phase to be erroneous ([5] considers baseline length B, baseline orientation α and radar wavelength). In this thesis, we will not consider the influence of an error in radar wavelength, which is considered to change only slowly and therefore to be constant throughout the scene.

Baseline errors are introduced into the interferogram in the following processing steps:

- flat-Earth phase subtraction,
- topographic phase subtraction, either performed using an external DEM, or the three-pass method.

Let us assume in the following considerations that the value of the look angle Θ is error-free. Its value is much more accurate due to the centimeter-scale orbit errors and the distance between the satellite and the Earth which is more than 800 km.

4.1 Flat-Earth Phase Subtraction

At the beginning, let us consider an Earth surface without topography, i.e. the reference ellipsoid itself. In this case, $\Theta = \Theta_0$ in formula (2.8).

The frequency of residual fringes in the range direction is (according to formula (2.8) where we neglect the error influence Φ_{err} and assume $\Phi_{tpg} = 0$)

$$f_r = \frac{d\Delta\Phi}{dr} = \frac{d\Delta\Phi}{d\Theta}\frac{d\Theta}{dr}, \tag{4.7}$$

where r is the distance (in meters) between the actual resolution cell and the satellite (*slant range*). It is a linear function of the position of the pixel in the image. The second term only represents the reference body, the (approximate) height of the satellite above it. The first term can be written as (according to formula (2.8))

$$f = \frac{d\Delta\Phi}{d\Theta} = -\frac{4\pi}{\lambda}B\cos(\Theta - \alpha) = -\frac{4\pi}{\lambda}\left(B_h\cos\Theta + B_v\sin\Theta\right) = -\frac{4\pi}{\lambda}B_\perp. \tag{4.8}$$

The second term may be written as

$$\frac{d\Theta}{dr} = -\frac{\cos\gamma}{\sin\Theta}\frac{R}{r(R+h)}; \tag{4.9}$$

meaning of the γ angle is clear from figure 4.2.

It is clear from formula (4.5) that the value of the perpendicular baseline changes from the near to far range. According to formula (4.5), the sign of the perpendicular baseline

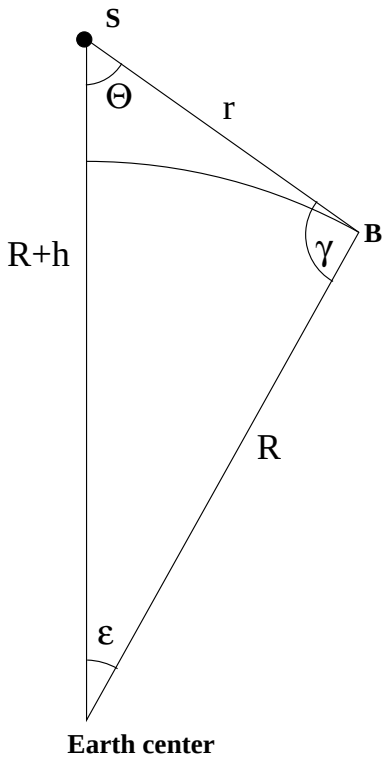

Figure 4.2: Configuration for derivation of $\frac{d\Theta}{dr}$.

may also change between the near and far range, although this case is quite improbable. The configuration is illustrated in figure 4.3.

In the cases a and b of figure 4.3, the frequency of the flat-Earth fringes is almost constant (i.e. the flat-Earth phase is almost linear). But for case a, the frequency has a different sign than for the case b. On the other hand, for the case c, the flat-Earth phase does not change linearly with the change of the look angle Θ and the frequency therefore changes its sign. The flat-Earth phase is detailed in figure 4.4.

From figure 4.4, it is clear that the flat-Earth phase changes with the change of the look angle. Fortunately, the look angle only changes by approx. $5\,^\circ$ throughout the scene, and if the value of baseline orientation α is distant from the values of $\Theta \pm \frac{\pi}{2}$, the frequency can be considered almost constant throughout the image. However, this is not the case for $\alpha \approx \Theta \pm \frac{\pi}{2}$ where the flat-Earth phase changes only slowly and it is useless to compute fringe frequency (note the range of the look angle in figure 4.4c). However, this is a scarce case and we have not encountered it yet.

More accurately, the fringe frequency changes throughout the image (the function contains a cosine). However, scene crops are often processed instead of the entire scene, causing a smaller error when the first-order terms are neglected.

If a component of the baseline is inaccurate, the flat-Earth phase is different than expected. The flat-Earth phase, which must be subtracted from an interferogram before evaluating (or subtracting) the topography, is computed using the known (inaccurate) baseline parameters by formula (2.9), with the substitution of $\Theta_0 = \Theta$ (for the surface without topography).

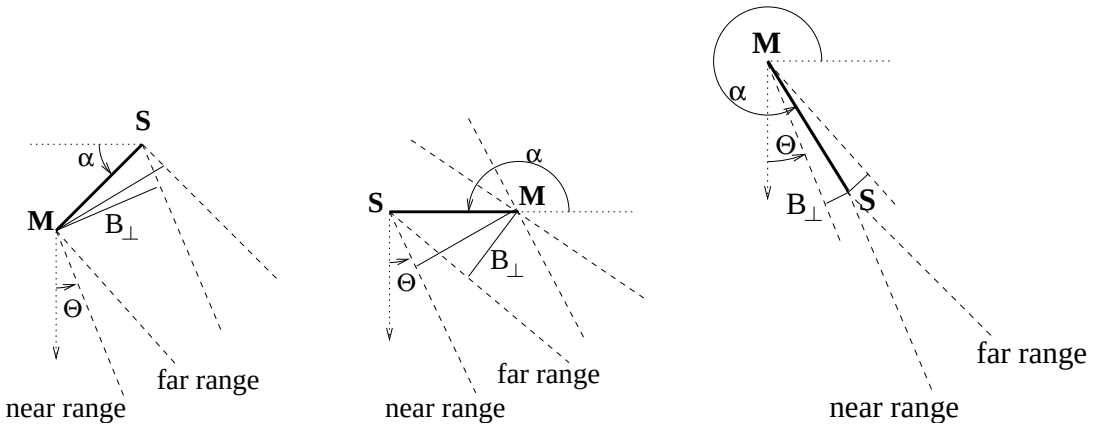

a.	b.	c.
$\Theta_{fr} - \frac{\pi}{2} < \alpha < \Theta_{nr} + \frac{\pi}{2}$,	$\Theta_{fr} + \frac{\pi}{2} < \alpha < \Theta_{nr} - \frac{\pi}{2}$,	$\Theta_{nr} + \frac{\pi}{2} < \alpha < \Theta_{fr} + \frac{\pi}{2}$ or $\Theta_{nr} - \frac{\pi}{2} < \alpha < \Theta_{fr} - \frac{\pi}{2}$,
$B_\perp > 0$	$B_\perp < 0$	either $B_\perp > 0$ or $B_\perp < 0$, depending on pixel position.

Figure 4.3: Baseline configuration with respect to the look angle. This figure is taken from [12].

When subtracting an inaccurate flat-Earth phase, some of the flat-Earth fringes stay in the interferogram: we will call these the *residual fringes* and label their frequency *df*. The value $df = 1$ means that the *residual phase* $d\Phi$ changes by 1 rad when the look angle Θ changes by 1 rad.

Let B_h and B_v be the real baseline components, and let $B_{hr} = B_h + dB_h$ and $B_{vr} = B_v + dB_v$, $B_{\parallel r} = B_\parallel + dB_\parallel$ be the reference baseline components, used for flat-Earth phase computation. Then, using formulas (2.8) and (2.9), we get the phase of the interferogram with the flat-Earth phase subtracted:

$$\Delta\Phi - \Phi_E = -\frac{4\pi}{\lambda}(B_\parallel - B_{\parallel r}), \tag{4.10}$$

$$\Delta\Phi - \Phi_E = \frac{4\pi}{\lambda}\left(dB_h \sin\Theta - dB_v \cos\Theta\right). \tag{4.11}$$

The residual fringe frequency *df* (which should be 0 ideally) is therefore

$$df = \frac{d(\Delta\Phi - \Phi_E)}{d\Theta} = \frac{4\pi}{\lambda}\left(dB_h \cos\Theta + dB_v \sin\Theta\right) = \frac{4\pi}{\lambda} dB_\perp. \tag{4.12}$$

where $dB_\perp$ is the perpendicular (with respect to the radar ray) component of the error baseline vector. The situation is illustrated in figure 4.5.

Formula (4.12) suggests that the residual fringe frequency does not depend on the baseline itself, but only on the perpendicular baseline error vector $dB_\perp$. That means that the residual phase depends on the error baseline orientation angle β in the same way as the

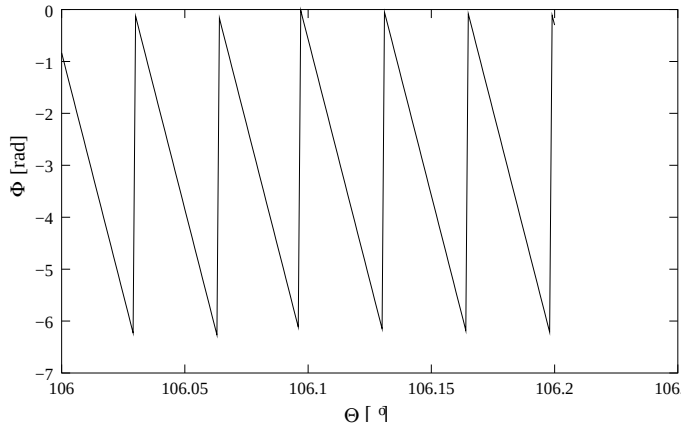

a ($\alpha = 0\,^\circ$)

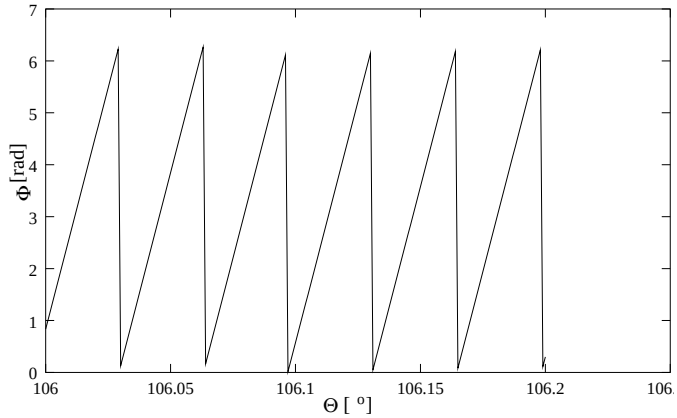

b ($\alpha = 180\,^\circ$)

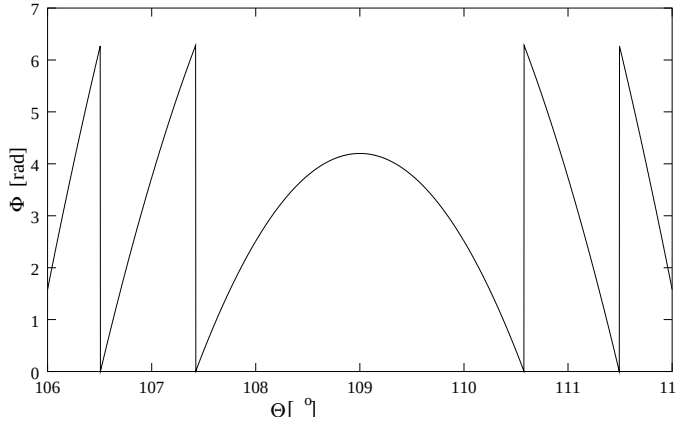

c ($\alpha = 109\,^\circ$)

Figure 4.4: The (wrapped) flat-Earth phase for various orientation angles α and baseline length $B = 50$ m. To be more illustrative, the look angle Θ varies in the interval of $\langle 16.0\,^\circ; 16.2\,^\circ \rangle$ for the cases *a*, *b*, and $\langle 16.0\,^\circ; 22.0\,\circ \rangle$ for the case *c*. This figure is taken from [12].

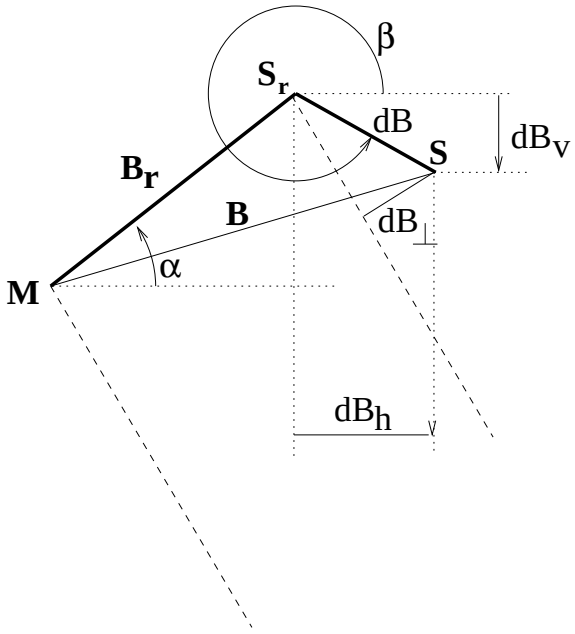

Figure 4.5: The baseline and its error.

flat-Earth phase itself depends on α (see figure 4.4). However, the orientation of the baseline error is never known and therefore the form of the residual phase or the number of fringes cannot be evaluated in advance.

The function of the frequency as dependent on the slant range r may be found in figure 4.6 for various values of the error baseline orientation β and $dB = 16.2$ cm (will be explained later). The function is valid for Earth approximation by sphere ($R = 6380$ km, $h = 800$ km).

From figure 4.6, it can be seen that the frequency change is the fastest for the worst case (baseline is perpendicular to the ray) and is only small for the best case (the baseline is parallel to the ray). We can conclude that the frequency changes almost linearly throughout the interferogram; that means that the phase depends on the slant range quadratically.

4.2 Flat-Earth Phase in the 3-pass Method

Although section 4.1 dealt with the flat-Earth phase subtraction in an interferogram without topography, the same applies to the interferogram in which the topography is subtracted with the use of an external DEM (two-pass method). This section deals with the case where the topography is subtracted using three-pass method. However, we will only deal with the flat-Earth phase.

Again, let us consider an interferogram where there is no topography; however, we will subtract it.

The residual phase of the defo interferogram is according to (4.10)

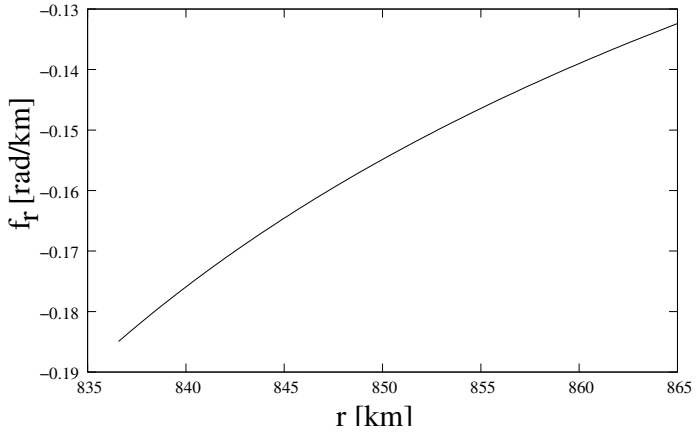

a. $\beta = 18.5\,^\circ$ (worst case)

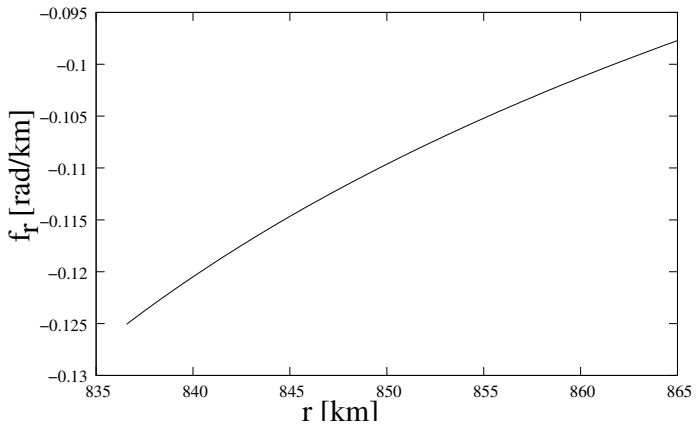

b. $\beta = 63.5\,^\circ$

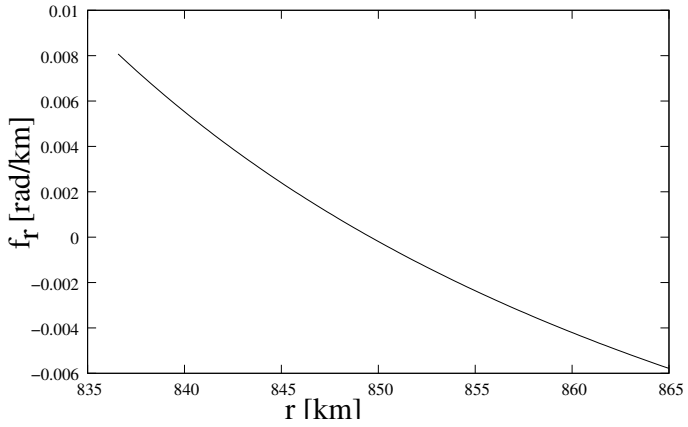

c. $\beta = 108.5\,^\circ$ (best case)

Figure 4.6: The residual fringe frequency as dependent on the slant range for different values of error baseline orientation; $dB = 22.8$ cm. For all functions, $16\,^\circ \leq \Theta \leq 21\,^\circ$ (the entire scene).

$$\Phi_{defo} = -\frac{4\pi}{\lambda}(B_{\|defo} - B_{\|rdefo}) = \frac{4\pi}{\lambda}\left(dB_{hdefo}\sin\Theta - dB_{vdefo}\cos\Theta\right), \tag{4.13}$$

and the residual phase of the topo interferogram is

$$\Phi_{topo} = -\frac{4\pi}{\lambda}(B_{\parallel topo} - B_{\parallel rtopo}) = \frac{4\pi}{\lambda}\left(dB_{htopo}\sin\Theta - dB_{vtopo}\cos\Theta\right). \tag{4.14}$$

According to (2.19), the phase of the differential interferogram is

$$\Phi_{\Delta r} = \Phi_{defo} - p_r\Phi_{topo}, \tag{4.15}$$

where $p_r = \frac{B_{\perp rdefo}}{B_{\perp rtopo}}$, while $p = \frac{B_{\perp defo}}{B_{\perp topo}}$. The residual phase of the differential interferogram is then

$$d\Phi_{\Delta r} = d\Phi_{defo} - p_r d\Phi_{topo}, \tag{4.16}$$

If the perpendicular baselines of both pairs are large enough so that $dB_\perp \ll B_\perp$, and the ratios $\frac{dB_\perp}{B_\perp}$ can be neglected for both pairs, formula (4.16) may be rewritten as

$$d\Phi_{\Delta r} = d\Phi_{defo} - p d\Phi_{topo}. \tag{4.17}$$

We will not consider the case of such a small perpendicular baseline, for which this formula cannot be used.

The frequency of residual fringes therefore is

$$df_{3-pass} = \frac{d\Phi_{\Delta r}}{d\Theta} = f_{defo} - p f_{topo}. \tag{4.18}$$

4.3 Topographic Phase Subtraction – 2-pass Method

The topographic phase to be subtracted (in the case of external DEM) can be figured out using formulas (2.11) and (2.14) (the function is almost linear):

$$\frac{d\Phi}{dh} = -\frac{4\pi}{\lambda}B_\perp\frac{1}{R_M\sin(\Theta+\varepsilon)}. \tag{4.19}$$

Now, we will again analyze the influence of imprecise orbits and DEM errors on the interferogram. The procedure will be similar to the case of the flat-Earth phase: for topography subtraction, the $B_{hr} = B_h + dB_h$ and $B_{vr} = B_v + dB_v$ baseline parameters are used. Also, the difference between the real height h above the reference surface and the DEM height $h_r = h + dh$ are considered.

The real topographic phase is (according to (4.19))

$$\Phi_{tpg} = -\frac{4\pi}{\lambda}\left(B_h\cos\Theta + B_v\sin\Theta\right)\frac{1}{\sin(\Theta+\varepsilon)R_M}h, \tag{4.20}$$

and the reference topographic phase (to be subtracted) is

$$\Phi_{tpgr} = -\frac{4\pi}{\lambda}\left((B_h + dB_h)\cos\Theta + (B_v + dB_v)\sin\Theta\right)\frac{1}{\sin(\Theta+\varepsilon)(R_M + dR_M)}(h + dh). \tag{4.21}$$

The residual phase therefore is

$$d\Phi_{tpg} = \frac{4\pi}{\lambda}\frac{1}{\sin(\Theta+\varepsilon)R_M}\left((B_\perp\left(dh - \frac{dR_M}{R_M}h\right) + dB_h\cos\Theta h + dB_v\sin\Theta h\right) \tag{4.22}$$

with the assumption $\frac{1}{1+x} \approx 1 - x$ for $x \ll 1$ and neglecting the second and higher order terms.

The term of formula (4.22) containing dh represents the DEM error, and the other terms include the orbit error influence: the higher the point above the reference ellipsoid, the more the phase is influenced.

In formula (4.22), dR_M is a function of dB_v and dB_h and should be accounted for together with other influences; however, the ratio $\frac{dR_M}{R_M}$ is very small and we will therefore neglect it.

4.4 Topographic Phase Subtraction — 3-pass Method

Now, we will consider the deformation and topographic interferograms, as described in section 2.3. Both interferograms have the flat-Earth phase subtracted and we consider the case that no deformations occured, i.e. $\Delta_r = 0$.

The phase of the differential interferogram is (according to formula (2.19))

$$\Phi_{dif} = \Phi_{defo} - \frac{B_{hrdefo}\cos\Theta + B_{vrdefo}\sin\Theta}{B_{hrtopo}\cos\Theta + B_{vrtopo}\sin\Theta}\Phi_{topo} = \Phi_{defo} - p_r\Phi_{topo}, \tag{4.23}$$

where index r again means the reference baseline components. Considering $B_{hri} = B_{hi} + dB_{hi}$ and $B_{vri} = B_{vi} + dB_{vi}$ where i can be "defo" or "topo", we can write according to formula (2.10)

$$\Phi_{dif} = \frac{4\pi}{\lambda}d\Theta\left[dB_{hdefo}\cos\Theta + dB_{vdefo}\sin\Theta - p\left(dB_{htopo}\cos\Theta + dB_{vtopo}\sin\Theta\right)\right] \tag{4.24}$$

where again

$$p = \frac{B_{\perp defo}}{B_{\perp topo}} \tag{4.25}$$

and with the assumption of $\frac{1}{1+x} \approx 1 - x$ for $x \ll 1$ and neglection of second and higher order terms. Using formulae (2.14) and (2.11) we can write (with the approximation $\sin d\Theta = d\Theta$)

$$\Phi_{dif} = \frac{4\pi}{\lambda} \frac{h}{R_M \sin(\Theta + \varepsilon)} \left[dB_{hdefo} \cos\Theta + dB_{vdefo} \sin\Theta - p \left(dB_{htopo} \cos\Theta + dB_{vtopo} \sin\Theta \right) . \right] \tag{4.26}$$

In this formula, the term containg $\frac{dR_M}{R_M}$ should appear; however, it is neglected due to the same reason as before.

This formula suggests that, the shorter the deformation baseline and the longer the topographic baseline, the less the interferogram is influenced by baseline errors of the topographic pair. On the other hand, the deformation baseline errors remain the same.

4.5 Evaluation of the Influences

We will now evaluate the influence of the orbit errors on various interferograms. We will consider the satellite radial orbit error of $\sigma_r = 6$ cm and the across-track error of $\sigma_a = 15$ cm (see section 3.4) and we will use real values of baseline components. These values were computed by the DORIS software and are shown in table 4.1.

In the following text, we will consider the baseline errors of

$$\sigma_{B_h} = \sqrt{2}\sigma_a = 21 \text{ cm}, \tag{4.27}$$

$$\sigma_{B_v} = \sqrt{2}\sigma_r = 8.5 \text{ cm}. \tag{4.28}$$

The radar wavelength is $\lambda = 5.67$ cm.

In the following text, we will try to evaluate the RMS influence, i.e. the RMS frequency of residual fringes or the RMS residual phase of a differential interferogram. We will consider the baseline component errors dB_h and dB_v to be independent. However, this assumption is not true, but no covariance matrix of the orbit errors is available.

In addition, the orbit error (in all directions) contains, besides the random component, also a systematic component. Unfortunately, we do not know much about the rate of these components and we will assume (in accord with [12]) the orbit error to contain the random component only (the worst case for baseline accuracy).

4.5.1 Flat-Earth phase influence

Let us transfer the formula (4.12) to the RMS:

$$\sigma_f = \frac{4\pi}{\lambda} \sqrt{\sigma_{B_h}^2 \cos^2\Theta + \sigma_{B_v}^2 \sin^2\Theta}. \tag{4.29}$$

The evaluation of the flat-Earth phase influence computed according to formula (4.29) is summarized in table 4.2. First, both the terms are separated in order to find out which term influences larger error, and then they are summed up.

	topo pair	defo pair 1	defo pair 2
baseline length B[m]	120.4	98.7	42.8
baseline length change (absolute) [m]	2.0	2.3	3.7
baseline orientation α[°]	-5.3	13.2	130.4
baseline orientation change (absolute) [°]	0.005	0.27	3.5
horizontal baseline B_h[m]	119.9	96.1	-29.3
vertical baseline B_v[m]	-11.3	22.5	31.8
horizontal baseline change (absolute) [m]	2.0	2.3	7.4
vertical baseline change (absolute) [m]	0.1	0.0	1.8
perpendicular baseline $B_\perp$[m]	110	98.3	-15.9
parallel baseline $B_\parallel$[m]	49	9.3	-39.6
look angle (scene center) Θ[°]	18.6	18.6	18.5
height ambiguity h_a[m]	69	77.2	-471.3

Table 4.1: Baseline parameters for the available data. Baseline component values (except for changes) are related to the scene center. Baseline component changes are the differences at the time of acquisition of the first and last azimuth lines. (The baseline parameters change approximately linearly in time. There are approximately 30 points for the entire scene among which the position is interpolated.) The different look angle for the deformation pair 2 is probably caused by the fact that its master scene is acquired by ERS-1, while the master scene of the other two pairs is acquired by ERS-2.

	all pairs
σ_{B_h} term [rad/rad]	44.6
σ_{B_v} term [rad/rad]	5.4
total σ_f[rad/rad]	44.9

Table 4.2: The RMS of the residual fringe frequency σ_f after subtraction of the flat-Earth phase in a flat area. The RMS of the residual fringe frequency is independent of the perpendicular baseline, it only depends on the baseline errors.

However, this approach does not consider the dependence of the frequency of residual fringes on the baseline error orientation angle β (see figure 4.5). In formula (4.29), the angle β is implicit, coming from the expected accuracy of the individual components. The situation is illustrated in figure 4.7.

However, assessing the "worst-case" fringe frequency is not straightforward. Formula (4.12) suggests that the longer the perpendicular baseline error, the more residual fringes appear in the interferogram, and that the residual fringe frequency does not depend on any other parameter.

Formula (4.29) does not consider the error baseline orientation at all. It supposes the horizontal component to be approximately three times larger than the vertical one, but that does not respect the value of $dB_\perp$. The situation is illustrated in figure 4.7; the angle γ denotes the "implicit" RMS orientation of the error baseline vector.

However, the look angle $\Theta \approx 18.5\,^\circ$ is similar to the "implicit" orientation angle $\gamma \approx 21.8\,^\circ$.

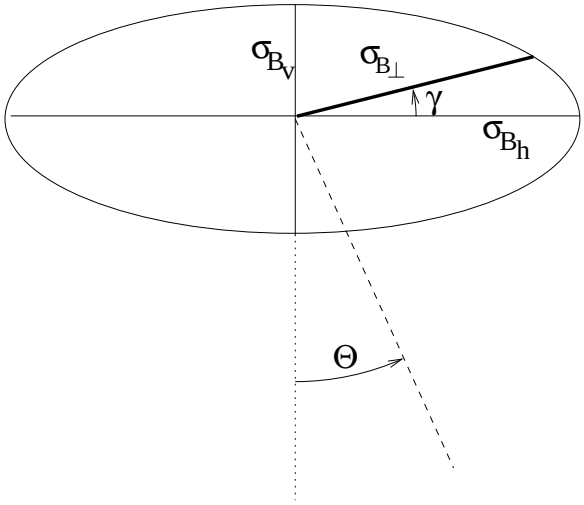

Figure 4.7: "Implicit" orientation of the error vector, $\gamma \approx 22\,^\circ$. Please note that the γ angle may be from the horizontal line both up and down, and also on the left side.

The "maximum RMS perpendicular baseline" (not illustrated in the image because it is very similar to $\sigma_{B_\perp}$) is

$$\sigma_{B_\perp max} = \sqrt{\sigma_{B_h}^2 \cos^2\Theta + \sigma_{B_v}^2 \sin^2\Theta} = 20.1 \text{ cm}, \tag{4.30}$$

corresponding to the maximal RMS fringe frequency

$$\sigma_f = \frac{4\pi}{\lambda} dB_\perp = 44.5 \text{ rad/rad}. \tag{4.31}$$

This is the worst case, very similar to the one evaluated using (4.29), due to the similarity of the angles γ and Θ. The best case is for $\beta \approx \Theta$ where the residual phase looks similar to the one illustrated in figure 4.4c.

Let us conclude here that the number of residual fringes does not depend on the baseline length and orientation (see formula (4.12)), but it only depends on the actual baseline errors.

According to figure 4.6, the RMS number of fringes (considering the worst-case error baseline orientation) in a scene is about three quarters ($\approx$ 4.8 rad) — scene width is approx. 30 km in slant range (see e.g. figure 4.6).

4.5.2 Flat-Earth phase subtraction – 3-pass method

Formula (4.18) cannot be transfered to RMS directly because of the interdependence of the baseline errors of the topo and defo pairs.

Let us suppose that the topo pair was acquired in the passes numbered 1 and 2, while the defo pair was acquired in passes numbered 1 and 3 (the pairs have common master). The ependence may be written as:

$$dB_{vdefo} = dr_3 - dr_1, \tag{4.32}$$
$$dB_{vtopo} = dr_2 - dr_1, \tag{4.33}$$
$$dB_{hdefo} = da_3 - da_1, \tag{4.34}$$
$$dB_{htopo} = da_2 - da_1, \tag{4.35}$$

where dr is the symbol for the radial orbit error, da is the symbol for the across-track error and the indices 1, 2, 3 denote the pass of the satellite.

That means that the RMS version of formula (4.17) looks like

$$\sigma_{f_{3-pass}} = \frac{4\pi}{\lambda}\sqrt{\sigma_{a_1}^2 t_{a_1}^2 + \sigma_{a_2}^2 t_{a_2}^2 + \sigma_{a_3}^2 t_{a_3}^2 + \sigma_{r_1}^2 t_{r_1}^2 + \sigma_{r_2}^2 t_{r_2}^2 + \sigma_{r_3}^2 t_{r_3}^2}, \tag{4.36}$$

where

$$t_{a_1} = (p-1)\cos\Theta, \tag{4.37}$$
$$t_{a_2} = -p\cos\Theta, \tag{4.38}$$
$$t_{a_3} = \cos\Theta, \tag{4.39}$$
$$t_{r_1} = (1-p)\sin\Theta, \tag{4.40}$$
$$t_{r_2} = p\sin\Theta, \tag{4.41}$$
$$t_{r_3} = -\sin\Theta. \tag{4.42}$$

Assuming the same RMS orbit errors for all scenes, formula (4.36) can be rewritten as

$$\sigma_{f_{3-pass}} = \frac{4\pi}{\lambda}\sqrt{2(p^2-p+1)\left(\sigma_a^2\cos^2\Theta + \sigma_r^2\sin^2\Theta\right)}. \tag{4.43}$$

Formula (4.43) suggests that the inaccuratelly subtracted flat-Earth phase can be partly eliminated by the 3-pass method. However, this applies only for the case where $0 \leq p \leq 1$.

The evaluation of the flat-Earth phase influence computed according to formula (4.36) is summarized in table 4.3.

Here we subtract the topo interferogram from each of the defo interferograms.

Table 4.3 suggests that the residual fringe frequency is much more caused by the across-track orbit error than by the radial one, similar to the last case. In comparison to table 4.2, it also suggests that the baseline error influence gets worse with another interferogram subtraction, especially in the case when the perpendicular baselines have different sign.

Same as in the last case, table 4.3 does not consider the orientation of the error baseline, i.e. considers the "implicit" orientation of both error baselines. As found out in section 4.5.1, this case is similar to the worst case for one interferogram.

However, the error may be larger when one of the error baselines is oriented in a different direction. In the worst case, when one error baseline is oriented in the "best" direction and the other in the "worst" one, the influence may be twice as large.

	defo pair 1 − topo pair	defo pair 2 − topo pair
p	0.89	-0.14
σ_{a_1} term [rad/rad]	3.55	35.90
σ_{a_2} term [rad/rad]	28.15	4.43
σ_{a_3} term [rad/rad]	31.47	31.47
σ_{r_1} term [rad/rad]	0.44	3.99
σ_{r_2} term [rad/rad]	3.10	0.44
σ_{r_3} term [rad/rad]	3.55	3.54
total $\sigma_{f_{3-pass}}$[rad/rad]	42.55	48.32

Table 4.3: Residual fringe frequency due to baseline errors, caused by inaccurate flat-Earth phase subtraction in 3-pass method. All the values are absolute.

4.5.3 Topographic phase subtraction – 2-pass method

Let us transfer formula (4.22) to RMS (with neglection of the dR_M error which was discussed above):

$$\sigma_\Phi = \frac{4\pi}{\lambda}\frac{1}{\sin(\Theta+\varepsilon)R_M}\sqrt{B_\perp^2\sigma_h^2 + \cos^2\Theta h^2\sigma_{B_h}^2 + \sin^2\Theta h^2\sigma_{B_v}^2}; \tag{4.44}$$

here we also assume that the DEM error dh is independent of the orbit errors dB_h and dB_v, which is true because the DEM was not used for orbit determination.

The evaluation of the topographic phase influence computed according to formula (4.44) is summarized in table 4.4.

Here we also consider $h = 1000$ m and $\sigma_h = 10$ m (which is approximately the accuracy of the SRTM DEM, which we use), $R_M \approx 830$ km (at the scene center) and $\Theta + \varepsilon \approx 23\,°$.

However, the height error RMS σ_h depends on the DEM used: we use an interferometric DEM (acquired in X and C bands) which should be the most suitable one for interferometric applications (although it may contain errors due to errors in phase unwrapping etc.). In the case of using a DEM measured by geodetic methods, the errors should be larger because the geodetic methods measure the Earth surface, while the interferometry (in C band) considers e.g. the tree-tops in vegetated areas.

	topo pair	defo pair 1	defo pair 2
σ_h term [rad]	0.75	0.67	0.11
σ_{B_h} term [rad]	0.14	0.14	0.14
σ_{B_v} term [rad]	0.02	0.02	0.02
total [rad]	0.76	0.68	0.18

Table 4.4: The interferogram phase error due to baseline errors, caused by inaccurate subtraction of the external DEM phase.

The subtraction of the topographic phase with an inaccurate baseline parameters also causes a trend in the range direction, but this trend is very small, less than one hundreth of the trend evaluated for the flat-Earth phase. Therefore, we will not evaluate it here.

As seen from table 4.4, the DEM error influences the residual phase much more than orbit errors, and also that the interferogram is more influenced by the across-track error than by the radial error. The reason for this is the value of the look angle Θ, which allows to transfer more of the across-track error than the radial error to the perpendicular baseline error. Only for a short perpendicular baseline (16 m) is the residual phase due to the DEM error smaller than the residual phase due to the orbit error.

The DEM error influence can be reduced easily during data selection: the shorter the baseline, the less the interferogram is influenced by the DEM error. This is usually the requirement for deformation mapping.

4.5.4 Topographic phase subtraction – 3-pass method

This case is similar to that analysed in section 4.5.2. That means that we must first transfer the baseline errors to the orbit errors of the individual passes.

The RMS version of formula (4.26) looks like

$$\sigma_{\Phi_{dif}} = \frac{4\pi}{\lambda}\frac{h}{R_M \sin(\Theta+\varepsilon)}\sqrt{\sigma_{a_1}^2 t_{a_1}^2 + \sigma_{a_2}^2 t_{a_2}^2 + \sigma_{a_3}^2 t_{a_3}^2 + \sigma_{r_1}^2 t_{r_1}^2 + \sigma_{r_2}^2 t_{r_2}^2 + \sigma_{r_3}^2 t_{r_3}^2}, \qquad (4.45)$$

where

$$\begin{aligned} t_{a_1} &= (p-1)\cos\Theta, && (4.46)\\ t_{a_2} &= -p\cos\Theta, && (4.47)\\ t_{a_3} &= \cos\Theta, && (4.48)\\ t_{r_1} &= (p-1)\sin\Theta, && (4.49)\\ t_{r_2} &= -p\sin\Theta, && (4.50)\\ t_{r_3} &= \sin\Theta. && (4.51) \end{aligned}$$

The formula (4.45) can be simplified assuming the same RMS orbit errors for all scenes,

$$\sigma_{\Phi_{dif}} = \frac{4\pi}{\lambda}\frac{h}{R_M \sin(\Theta+\varepsilon)}\sqrt{2(p^2-p+1)\left(\sigma_a^2\cos^2\Theta + \sigma_r^2\sin^2\Theta\right)}. \qquad (4.52)$$

The evaluation of the topographic phase influence computed according to formula (4.45) is summarized in table 4.5.

Here we also consider $h = 1000$ m, $R_M \approx 830$ km (scene center) and $\Theta + \varepsilon \approx 23\,^\circ$.

We subtract the topo interferogram from each of the defo interferograms.

The baseline inaccuracy also causes trend in the range direction, but this trend is very small, less than one hundreth of the trend evaluated for the flat-Earth phase. Therefore, we will not consider it here.

	defo pair 1 − topo pair	defo pair 2 − topo pair
p	0.89	-0.14
σ_{a_1} term [rad]	0.01	0.11
σ_{a_2} term [rad]	0.09	0.01
σ_{a_3} term [rad]	0.10	0.10
σ_{r_1} term [rad]	0.001	0.015
σ_{r_2} term [rad]	0.011	0.002
σ_{r_3} term [rad]	0.013	0.013
total [rad]	0.14	0.15

Table 4.5: The interferogram phase error due to baseline errors, caused by inaccurate subtraction of the topographic interferogram.

4.5.5 Comparison and conclusion

In the tables 4.2, 4.4 a 4.5, it can be seen that the influence of orbit errors caused by imprecise topography subtraction is small in comparison to imprecisely subtracted flat-Earth phase (let us remind that the topographic errors were computed for $h = 1000$ m, for smaller heights the error influence is even less). In addition, the three-pass method is more accurate because the errors originating from DEM errors are eliminated and also, there is no coregistration needed. But this only applies for the case where $0 \leq p \leq 1$.

In the opposite case, i.e. when the topographic baseline is shorter than the deformation baseline, the topographic heights are determined less accurately, compared to the accuracy used for topography subtraction. In this case, the term $p^2 - p + 1$ of formula (4.52) gets large and the accuracy worsens. The same applies for the case where defo and topo perpendicular baselines have different signs.

Let us add here that the residual phase errors (due to topography subtraction) cannot be determined in a real interferogram; however, a trend in the interferogram can be usually seen (sometimes, this trend causes real fringes if the errors are larger) and their presence can be used to correct the baseline. Another computation with the "right" baseline should eliminate the errors dependent on topography, too.

In practice, however, the relative heights are more important than the absolute ones: the orbit error only "scales" the heights. In a smooth terrain, this should not cause a problem.

Let us note here that most of the baseline errors do not depend on the baseline length and orientation, and therefore the influence cannot be eliminated by appropriate data selection. The only advice is to choose data with a short perpendicular baseline for deformation mapping using two-pass interferometry, or a short perpendicular baseline of the deformation pair and long perpendicular baseline of the topographic pair in case of three-pass interferometry.

4.6 Fringes in the azimuth direction

Fringes in the azimuth direction are not fringes themselves, but only a change of range fringe frequency during the image acquisition. That means that they are caused by

variability of orbit errors during the pass of the satellite.

These are usually not as large as the errors in the range direction; the orbit error does not usually change quickly — it contains a systematic error (for such a short period of time). However, the error characteristics are not known.

4.7 Atmospheric fringes

The fringes need not be caused only by orbit errors: they can also be caused by a difference in atmospheric delay in different parts of the image. Let us avoid the cases where a front edge appears in the image or when a storm occurs during scene acquisition. In the other cases, the atmospheric delay changes slowly (see [12]) and cannot be distinguished from the influence of orbit errors.

The change of atmospheric features may occur in both directions with the same probability; however, atmospheric fringes appear more probably in the range direction. This is caused by the different path length through the atmosphere at close and far range (see [13]).

Because both influences (orbital and atmospheric) cannot be usually distinguished in an interferogram, they are eliminated together. Rather than seeking for the "correct" baseline, an *artificial* baseline resulting in an interferogram without residual fringes is determined [29].

Chapter 5

Error-influenced Interferograms

This chapter analyses the influence of orbit errors on real interferograms. It deals not only with the interferogram slope, but also with the shift of the scenes with respect to each other and with the shift of the interferogram (i.e. of the master scene) with respect to SRTM DEM.

The interferometric pairs, described in table 4.1 – topo pair, defo pair 1 and defo pair 2, are formed by three scenes, and their acquisition parameters are shown in table 5.1.

pair	master acquisition date	master sat.	slave acquisition date	slave sat.
topo	March 8^{th}, 1999	ERS-2	March 7^{th}, 1999	ERS-1
defo 1	March 8^{th}, 1999	ERS-2	December 28^{th}, 1998	ERS-2
defo 2	March 7^{th}, 1999	ERS-1	December 28^{th}, 1998	ERS-2

Table 5.1: Particular scenes used for each pair as described in chapter 4. More details about the pairs can be found in table 4.1.

5.1 Scene shift

An easily recognized error is the shift between the two scenes, processed into an interferogram. It is natural that two scenes are shifted, but the shift may be computed from the satellite positions. On the other hand, it can also be evaluated by comparing the magnitudes of the images (2D correlation). Both procedures are performed in DORIS: the precise orbits should allow computing the shift with the precision of several tens of pixels, which is a parameter of the following procedure, allowing to compute the shift with the precision of 1 to four pixels. In order to get a more precise offset, small crops of the scene are oversampled and correlated. The differences between the shift computed from the satellite positions and the magnitude correlation (without oversampling) is shown in table 5.2.

In table 5.2, one can see that the error of the deformation pair 1 is much smaller than for the other two pairs. We attribute this to the fact that both the topo and the defo 2

computation using	orbits		correlation		difference	
pair	azimuth	range	azimuth	range	azimuth	range
topo	-39	-7	-251	-7	-212	0
defo 1	27	-2	43	-1	16	1
defo 2	66	5	289	5	223	0

Table 5.2: The differences in scene shift computed using precise orbits and image correlation for the processed pairs (using image magnitude). All the values are in pixels. The values may change by a few pixels depending on the scene crop. The values refer to the original pixels, no the multilooked ones.

pair contain the ERS-1 scene, while the defo 1 pair contains both ERS-2 scenes (see table 5.1).

Let us also notice that the image position is good in range, but the azimuth position is errorneous. As described in section 3.4, the along-track (timing) error is the largest of all the orbit error components.

Although precise orbits are no more available for ERS-1 in 1999 (the orbits used are only fast-delivery orbits), their error should not be large enough to cause shifts about 1 km. We attribute this error to a timing bias between ERS-1 and ERS-2.

However, as written above, the scene shift is not significant for interferometry, because the images are coregistered using image magnitude and cut off in order to contain the same area.

5.2 Residual fringes

Figures 5.1, 5.2 and 5.3 show the residual fringes caused by inaccurate flat-Earth phase subtraction (as derived in chapter 4). The topography was either subtracted using the SRTM DEM (figures 5.1 and 5.2) by two-pass interferometry, or using the topo pair by three-pass interferometry (figure 5.3). Unfortunately, we were unsuccessful in processing the defo pair 2 for this large scene (probably due to the large convergence of the orbits, see table 4.1).

The residual fringe frequency in the range direction is approximately four times larger than the estimate in table 4.2 (for this scene crop, the RMS worst-case residual frequency is approximately half a fringe (see section 4.1)). We may also attribute the error to the larger ERS-1 orbit error (for the topo pair imaged in figure 5.2). However, a similar trend can also be seen in figure 5.1 where no ERS-1 scene was processed.

We cannot attribute such a large error to atmospheric delay. The criteria for data selection were very strict, selecting only acquisition dates without rain three days before.

The differential interferogram (figure 5.3), created from the defo 1 and topo pairs, is almost without residual fringes. Please note that the fringes in the range direction of both defo 1 and topo pairs (figures 5.1 and 5.2) are in the same direction, although the azimuth fringes are in the opposite direction. After subtraction, range fringes are eliminated except for a small fraction, but the azimuth fringes add up.

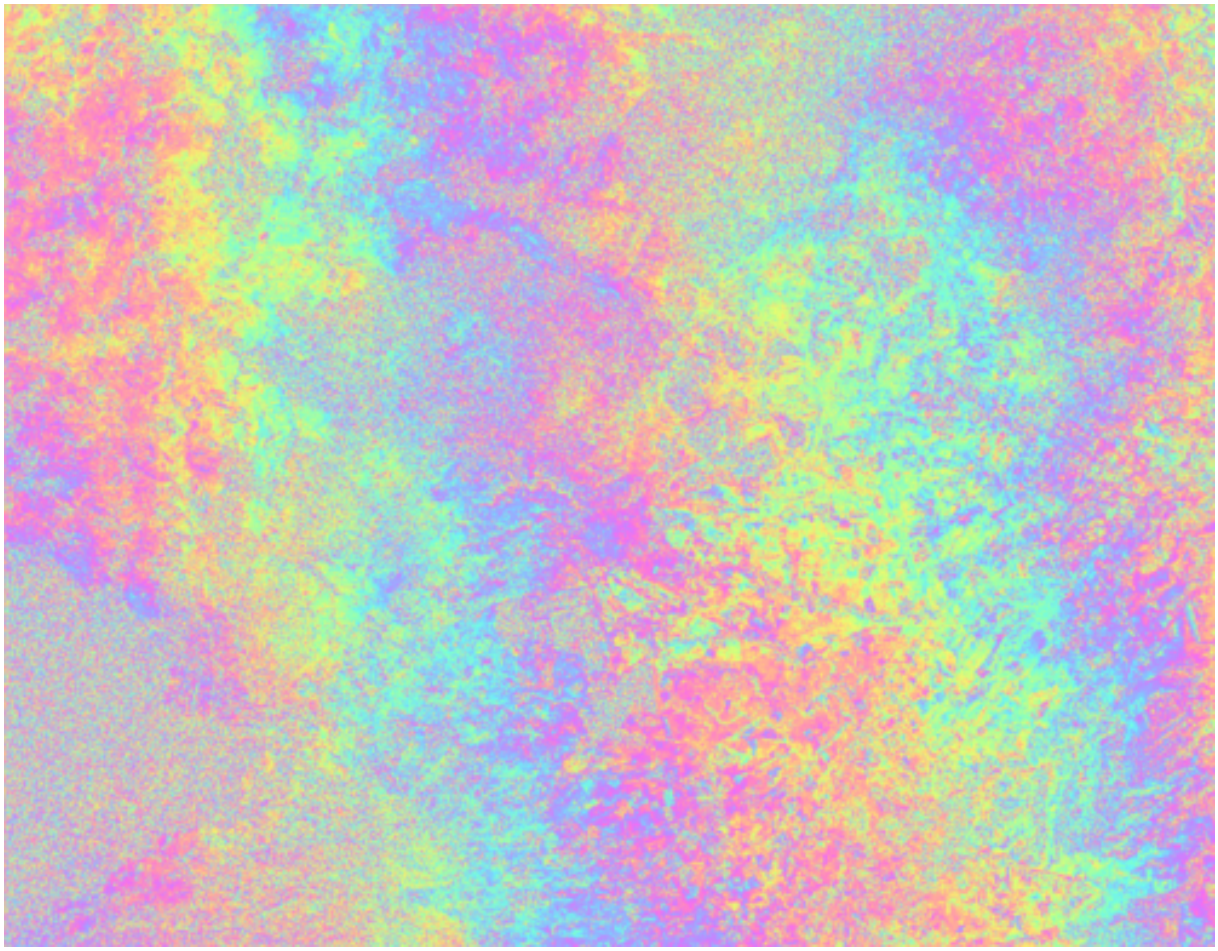

Figure 5.1: The influence of orbit errors on the interferogram with subtracted topography using SRTM DEM (defo pair 1, as described in table 4.1). There are more than two residual fringes in the range direction and less than half a fringe in the azimuth direction. This interferogram contains 4096 pixels in the range direction and 16384 pixels in the azimuth direction, i.e. it covers almost a half of the scene.

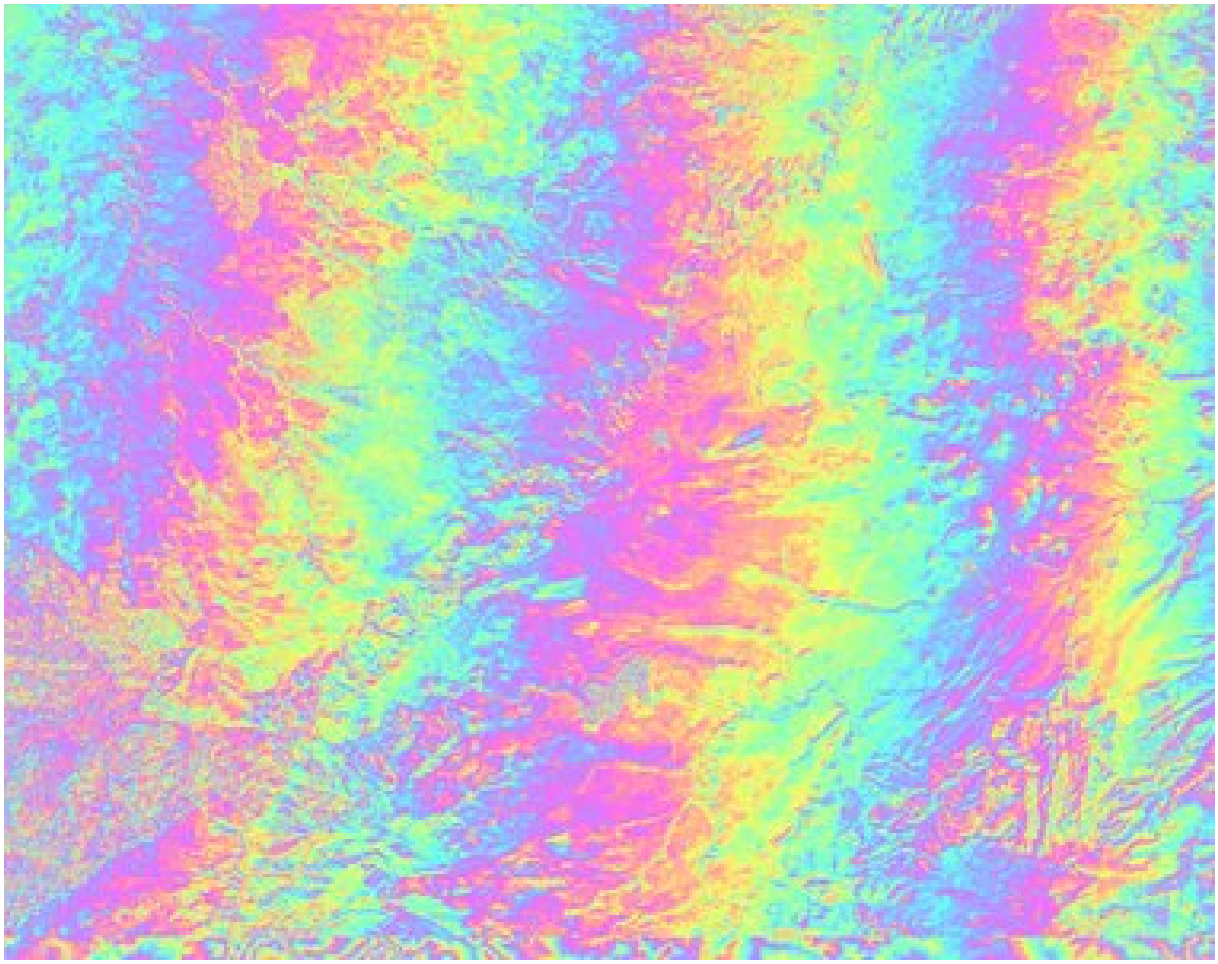

Figure 5.2: The influence of orbit errors on the interferogram with subtracted topography using SRTM DEM (topo pair, as described in table 4.1). There are more than three residual fringes in the range direction, the azimuthal fringe is minor. This interferogram contains 4096 pixels in the range direction and 16384 pixels in the azimuth direction, i.e. it covers almost a half of the scene.

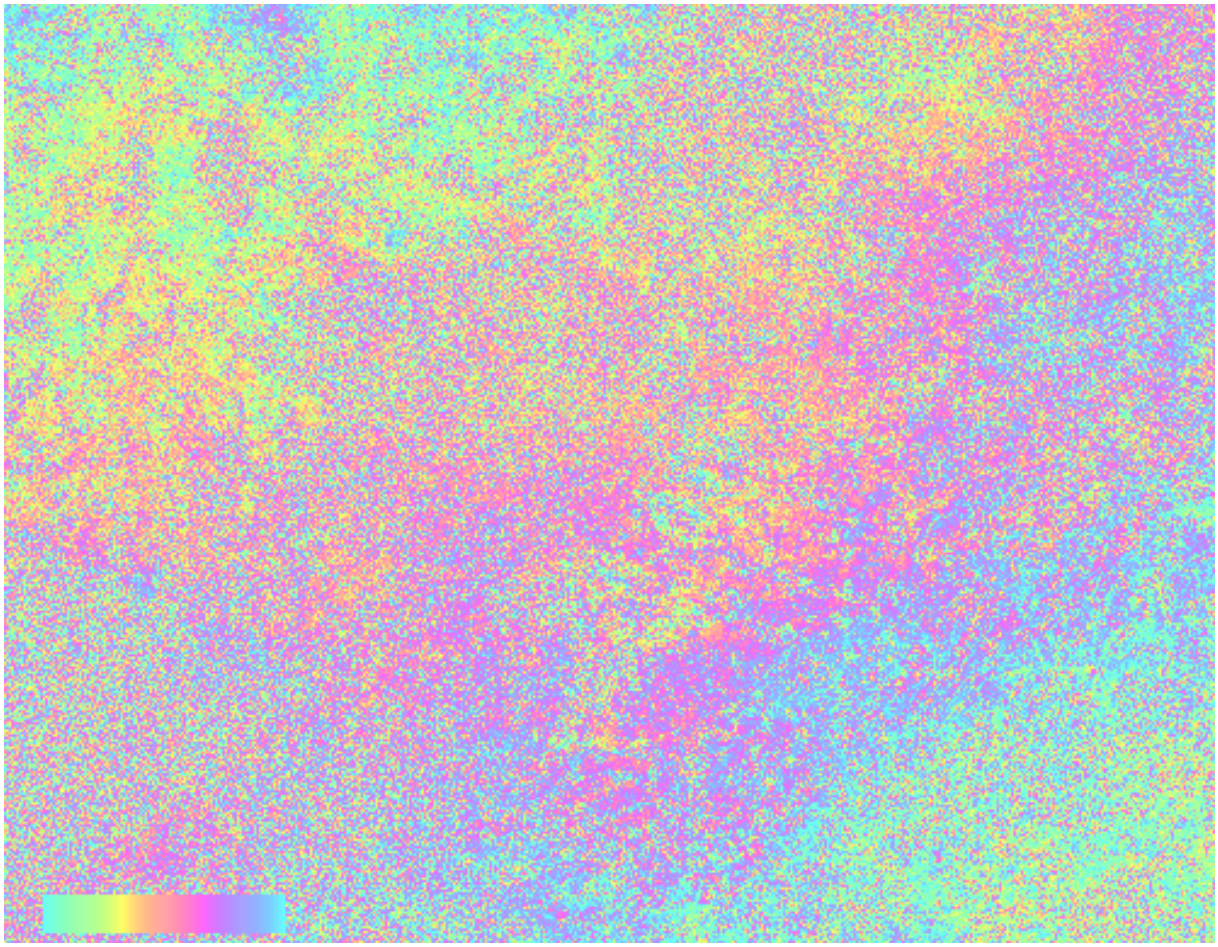

Figure 5.3: The influence of orbit errors on the interferogram with subtracted topography using the three-pass method (defo 1 and topo pairs, as described in chapter 4). There is less than one fringe in both directions, the interferogram looks as if it is sloped. This interferogram contains 4096 pixels in the range direction and 16384 pixels in the azimuth direction, i.e. it covers almost a half of the scene.

5.3 Interferogram shift

In order to subtract the topography from an interferogram with the two-pass method, an external DEM of the same area must be used. In a flat area, the DEM may be less precise or even neglected, but in a mountainous area, the DEM must be accurately coregistered with the interferogram.

First, the DEM is converted to the radar coordinate system, i.e. the distance between the satellite and the reference point on the Earth surface. The distance is then converted to phase and wrapped. That means that the converted DEM does not contain any reflectivity (magnitude) information and therefore regular coregistration, which uses the magnitude information, cannot be used.

[31] attempts to create an artificial magnitude image with the use of information about (approximate) satellite positions and terrain slopes (taking advantage of radar artifacts, such as foreshortening, layover and shadow) and then tries to perform magnitude coregistration with the interferogram (let us remind here that magnitude of the interferogram is a product of the magnitudes in the individual scenes). However, the artificial magnitude is different from the natural one except for mountainous areas. The authors conclude that the coregistration works even in flat areas with elevation differences of less than 100 m. However, we did not try this approach.

Table 5.3 illustrates the shift of the interferograms with respect to the radarcoded SRTM DEM. These shifts were obtained manually (comparing the phase images) and then improved by trial-and-error (the DEM phase was subtracted from the interferogram and the resulting interferogram was compared to the previous iteration). We estimate the precision of this shift to be about 5 pixels in range direction and 25 pixels in the azimuth direction (before multilooking).

Let us stress here that the interferogram represents the right values, while the DEM was radarcoded using the known (imprecise) orbit parameters.

pair	azimuth shift	range shift
topo	-815	70
defo 1	-870	79
defo 2	-1080	87

Table 5.3: The interferogram shift of the various processed pairs with respect to the radarcoded SRTM DEM. All values are in pixels of the original scene (i.e. not multilooked). The shift is approximately constant in the whole image. The shift of the defo 2 pair was evaluated in a different scene crop. In addition, due to a very large value of height ambiguity for the defo 2 pair, the values for defo 2 are difficult to determine and may therefore contain an error of at most 10 pixels in range and 100 pixels in azimuth.

Table 5.3 suggests that the shift of the processed interferogram not only depends on the position of the master satellite, but also on the position of the slave satellite. This is natural because the DEM is radarcoded using the information about both satellite positions; however, the most error is caused by the master satellite position error.

Chapter 6

Detrending the Interferograms

In this chapter, we will describe methods to detrend the interferogram. The trend is caused by the orbit errors, as described in chapters 4 and 5, only the flat-Earth phase is assumed (the trend caused by imprecise topography subtraction is neglectable). The simplest approach is to unwrap the residual phase and compute a plane (or quadric) which is "as close as possible" to the unwrapped surface, using the selected criteria.

However, this approach may have some problems:

- the decision whether to use all pixels for adjustment, or only those whose coherence is higher than a threshold;
- there may be a large amount of "wrong" pixels in the interferogram, causing the plane to be biased;
- the phase may be unwrapped incorrectly due to continuous low-coherent patches;
- plane subtraction is not exact (see figure 4.6).

The third problem is the most important: although we can make various decisions regarding the coherence of the points which are to be the adjustment input, there is no possibility to influence phase unwrapping. The SNAPHU program, which we use, is very good in unwrapping topographic surfaces (it also uses scene magnitude as an information source) but deformation interferograms are unwrapped without any apriori information; therefore, errors occur more often. Phase unwrapping is the least reliable step of the interferometric processing.

6.1 The `cpxdetrend` script

The `cpxdetrend` script is provided by the DEOS group at the Delft University of Technology as a supplement to the DORIS software. However, it is a script to be run in the MATLAB environment.

First, it tries to compute the number of fringes in both x and y directions. It uses Fast Fourier Transform (FFT); without oversampling the image first (which is not implemented

yet), the number of fringes computed is always integral (due to the discrete nature of FFT). FFT can only assess the frequency of the major signal in the image, therefore topography cannot be present in the image. In addition, the script cannot identify fringes which are not equally spaced (e.g. of the shape illustrated in figure 4.4c). Besides that, the script is not able to detect a part of a fringe.

On the other hand, the `cpxdetrend` script does not use FFT for elimination of the fringes, which allows to eliminate even a non-integral number of fringes or even a part of a fringe (in both x and y directions). Two planes are constructed using the fringe frequencies in the range and azimuth directions and then subtracted. Subtraction is performed (like in other cases) using complex-conjugate multiplication. However, if subtraction of a non-integral number of fringes is desired (which is our case), the number of fringes to be extracted must be entered manually and the value should be corrected after the trial.

The detrended version of the interferogram shown in figure 5.1 is shown in figure 6.1. Detrended version of the interferogram shown in figure 5.2 may be found in figure 6.2.

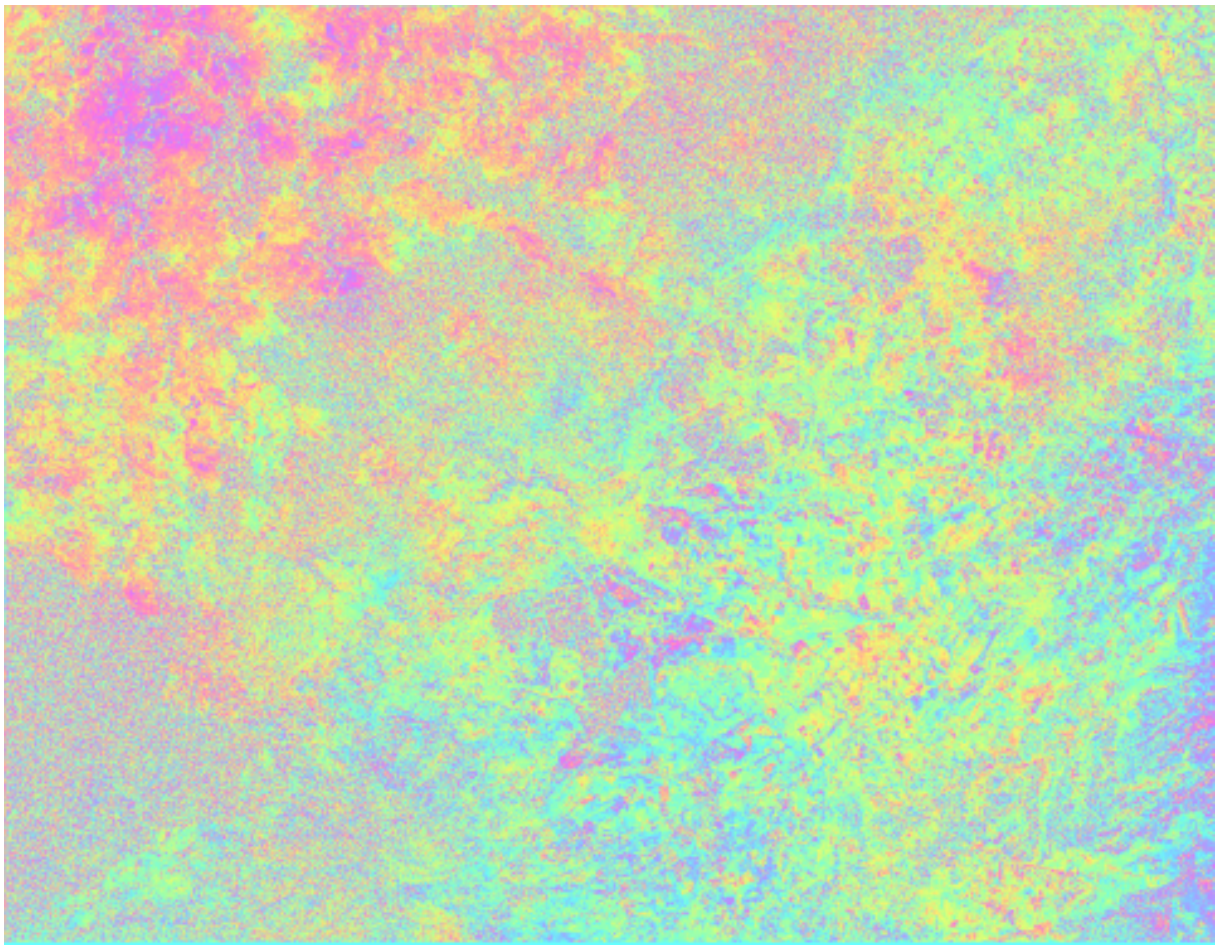

Figure 6.1: Interferogram processed from the defo 1 pair with subtracted topography using SRTM DEM. The interferogram was detrended using the `cpxdetrend` script. The script was run with the following parameters: -1.9 fringes in the range direction, and -0.3 fringes in the azimuth direction.

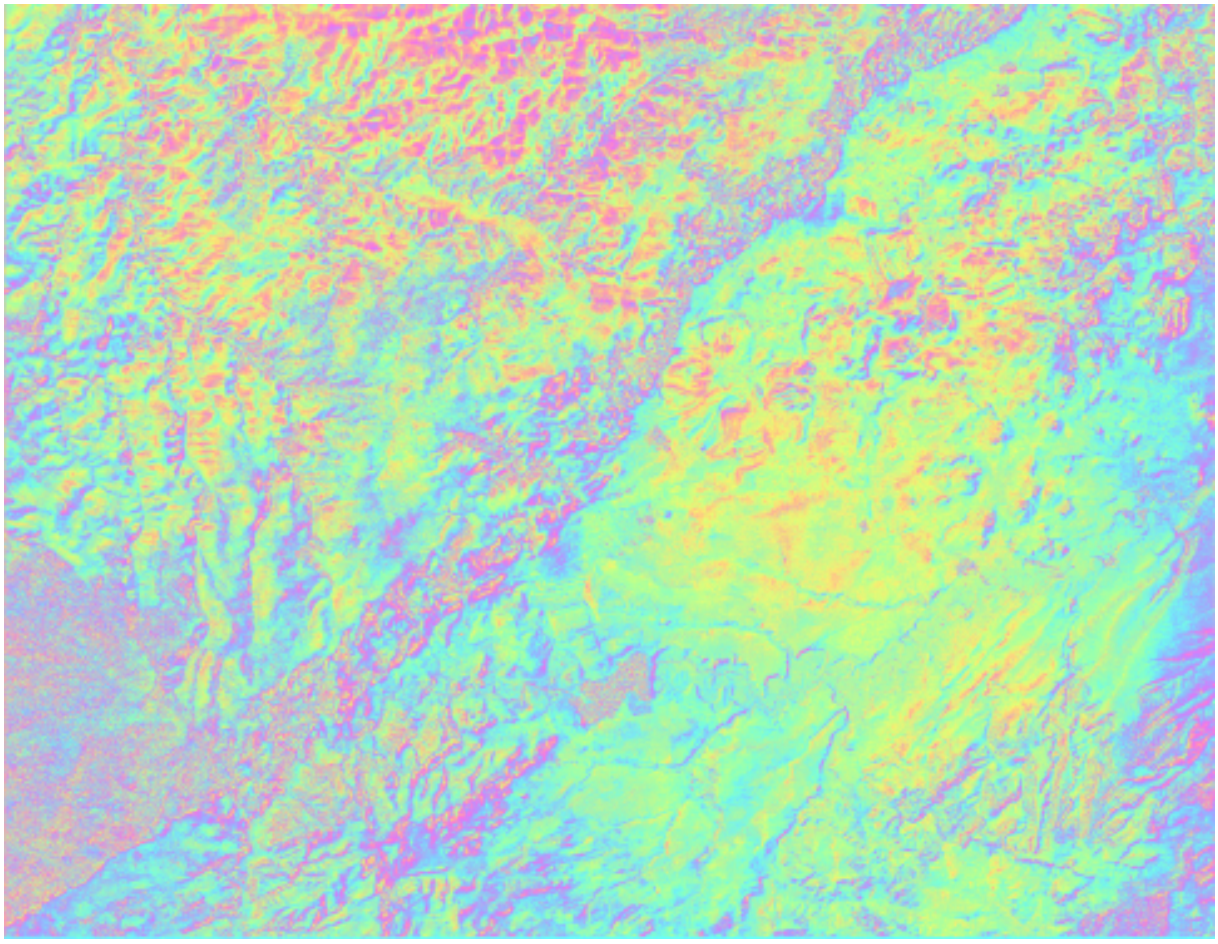

Figure 6.2: Interferogram processed from the topo pair with subtracted topography using SRTM DEM. The interferogram was detrended using the `cpxdetrend` script. Theoretically, the phase of this interferogram should be unique. The non-uniqueness may be caused by an imprecise coregistration of the image and DEM, by changes of the terrain during 1999–2000 (between acquisitions of the SRTM DEM and the scenes), or by deformations occuring during one day (improbable). Atmospheric delay change would have caused a long-wavelength trend in both azimuth and range directions. The script was run with the following parameters: -3 fringes in the range direction, and 0 fringes in the azimuth direction.

However, the `cpxdetrend` script can only eliminate a constant frequency, or a linear phase. After that, some trend may remain in the image, but this is no more linear and cannot be eliminated by another run of the `cpxdetrend`. This is a consequence of the simplicity of the method.

In cases where the perpendicular baseline is near zero, the phase looks like figure 4.4c. In this case, the `cpxdetrend` script fails entirely because the phase is no more linear and the sign of frequency changes. However, the phase changes very slowly in this case, and the fringes may not be seen at all for smaller crops.

In addition, the `cpxdetrend` script does not provide any information about how long the baseline should really be. We can conclude that the `cpxdetrend` script should be used for

making the deformation spots in the interferogram better detectable, but not for baseline correction.

6.2 Baseline correction with respect to residual fringes

In this section, we will try to adjust the orbit parameters according to the residual phase in the interferogram. In contrast to the above described `cpxdetrend` script, we will try not only to detrend the interferogram, but also to obtain more precise baseline parameters.

As noted above, the interferogram is only a relative measure, resulting in the fact that it is never possible to obtain correct values for both satellite positions. The only parameter to be adjusted is the baseline — i.e. we will consider the orbit of the master satellite to be correct and will only adjust the orbit of the slave satellite.

6.2.1 Adjustment according to [18]

This procedure is described in [18] and also in [12]. Suppose we have an interferogram and label its four corners A, B, C, D (see figure 6.3).

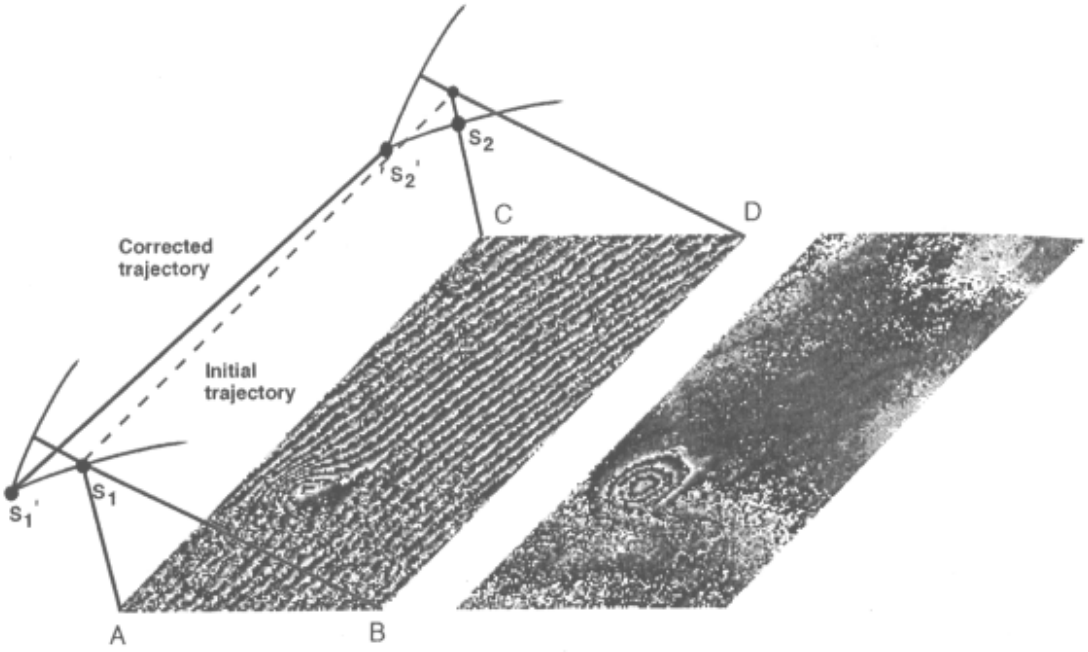

Figure 6.3: The illustration of the baseline adjusting procedure. This image was copied from [18]. Only a black-and-white copy of the article was available.

Let us first cite from [18]: *Here we count 15 fringes from point A to B, so the distance between satellite 1 and B should be lengthened by 15 times half the wavelength. If distance AB remains unchanged, the correct satellite position lies at the intersection of the two arcs at* S_1'*. Keeping A as a reference, we find that distance* DS_2 *should be lengthened (by 4 cycles) and distance* CS_2 *shortened (by 10 cycles), which puts the refined position at*

the end of the interferogram at S_2'. Using the refined trajectory and reprocessing the radar data suppresses orbital fringes.

The description is very strict here: the sign of the residual phase change (frequency) is not defined, although it is recognized. In addition, the sign of the distance changes to be adjusted also depends on the sign of the fringe frequency.

6.2.2 The critique described in [12]

Book [12] comments the above approach, and describes it more clearly: *In this approach, one satellite position is fixed, while the second one, indicated in figure* 6.4, *is changed in two steps. First, since the range distance $R_{2,nr}$ to the first pixel in range can be kept constant, the position of the satellite needs to be somewhere on curve 1. By counting the number of fringes between near-range and far-range, range vector $R_{2,fr}$ needs to be changed in length, denoted as step 1. Keeping this value for $R_{2,fr}$, the position of the satellite needs to be somewhere on curve 2. Therefore, in step 2, the position is moved to the cross-section of curve 1 and 2. Using the same approach in azimuth direction, residual azimuth fringes can be eliminated.*

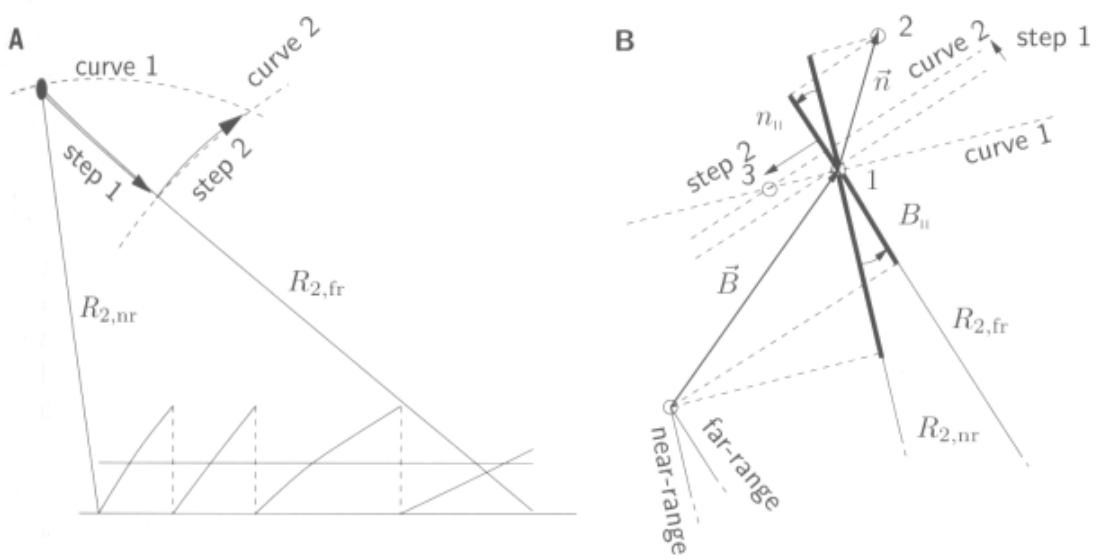

Fig. 4.24. (A) Correction of orbit error for the first range line in two steps,see Massonnet and Feigl (1998). **(B)** Difference between the true error vector $\vec{n}$ (position 2), and the position obtained with the method in (A) (position 3). The parallel components of $\vec{B}$ and $\vec{n}$ are denoted by the thick lines. Position 1 indicates the a priori position found by using (precise) orbital state vectors.

Figure 6.4: The illustration of the error in the approach described in [18]. This figure is copied from [12].

Although it seems that this approach solves for the error vector $\vec{n}$ this is in fact not totally true. In fact, the method corrects only for the change in the parallel component of the error vector $n_{\|}$

$$\delta n_{\parallel}(R_2) = n_{\parallel}(R_{2,fr}) - n_{\parallel}(R_{2,nr}),$$

which causes the residual fringes in the interferogram. The method does not correct for the perpendicular component of the error vector, $n_{\perp}$, and still leaves an error in the height conversion factor. In figure 6.4B *it is shown how this method fails finding the correct position of the satellite. The a priori position of the satellite is indicated as position 2. The error vector $\vec{n}$ points from position 1 to 2. As B is often much larger that n, the major part of the reference phase is decreasing with range, indicated by the boldly drawn parallel component of $\vec{B}$. The reference phase from this baseline can be eliminated totally. The orientation of the error vector $\vec{n}$ is not known, though. From the figure it is clear how $n_{\parallel}$ is also decreasing with range. The length change of $n_{\parallel}$ from near-range to far-range is directly related to the number of residual fringes in the interferogram.*

Since $n_{\parallel}(R_{2,nr})$ is unknown, we can only observe the residual fringes in the interferogram, which are equivalent to $\delta n_{\parallel}(R_2)$. In fact, we observe from the interferogram that $R_{2,fr}$ is too short by $\delta n_{\parallel}(R_2)$. Correcting for this error is indicated as step 1 in figure 6.4B. *Keeping $R_{2,nr}$ constant, the position that* [18] *would find will be the intersection of curve 1 and 2, indicated as position 3. It is clear from the figure that this method might eliminate the residual reference phase, but it decreases the perpendicular baseline $B_{\perp}$, whereas the correct solution increases $B_{\perp}$.*

6.2.3 Analysis of the procedure

For the analysis of the procedure, we will use the notation used in chapter 4. The baseline error vector is here $-dB$, because it is defined as

$$dB = B_r - B, \tag{6.1}$$
$$dB_{\perp} = B_{\perp r} - B_{\perp}, \tag{6.2}$$

where B is the correct baseline and B_r is the reference baseline used for reference flat-Earth phase computation. The residual fringe frequency (determined from the interferogram) is (4.12)

$$df = \frac{4\pi}{\lambda} dB_{\perp}.$$

This means that if $df > 0$, the residual reference phase grows throughout the interferogram and $dB_{\perp}$ is also positive.

The formula for flat-Earth phase subtraction looks like this (4.10):

$$\Delta\Phi - \Phi_E = -\frac{4\pi}{\lambda}(B_{\parallel} - B_{\parallel r}),$$

therefore if the residual phase grows, the absolute value of the reference flat-Earth phase should be smaller. However, as described in [12], the flat-Earth phase corresponds to

the parallel baseline, i.e. the difference between the distance between a point P and the master and slave satellites (formulas (2.4) and (2.9)) is:

$$B_{\parallel} = R_A - R_B = B\sin(\Theta_0 - \alpha) = -\frac{\lambda}{4\pi}\Phi_E.$$

This means that if the absolute value of the flat-Earth phase is too large at far range, the distance R_B between the slave satellite and the point at the far range should be lengthened with respect to the distance R_A. As noted above, the position of the master satellite A remains the same.

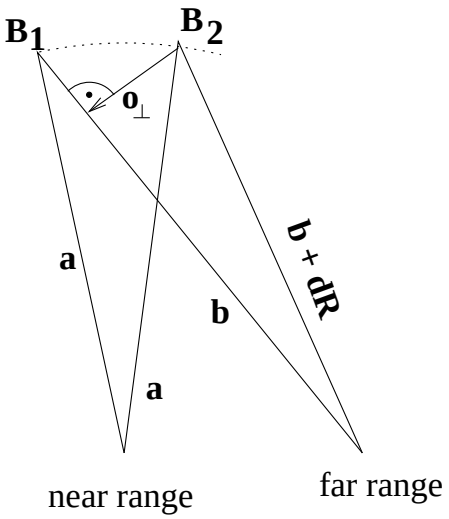

Figure 6.5: Change of the distance between the slave satellite and a far-range point with respect to the errorneous perpendicular baseline. Here, $dR < 0$ and $o_\perp < 0$.

Changing the distance between the point at the far range and the slave satellite may have two effects (see figure 6.5):

- if the distance is lengthened ($dR_B > 0$), $o_\perp > 0$,
- if the distance is shortened ($dR_B < 0$), $o_\perp < 0$,

where $o_\perp$ is the perpendicular part of the baseline adjustment. Here it applies that sign $(dB_\perp)$ = sign $(o_\perp)$, therefore the perpendicular part of the baseline is adjusted in the right direction (in contrast to [12]).

Now, let us analyse the adjustment in more detail, not only the sign, but also the value. The situation is illustrated in detail in figure 6.6.

For the satellite positions B_1 and B_2, the following equations apply:

$$x_1^2 + y_1^2 = x_2^2 + y_2^2 = a^2, \tag{6.3}$$
$$(x_1 - k)^2 + y_1^2 = b^2, \tag{6.4}$$
$$(x_2 - k)^2 + y_2^2 = (b - dR)^2, \tag{6.5}$$

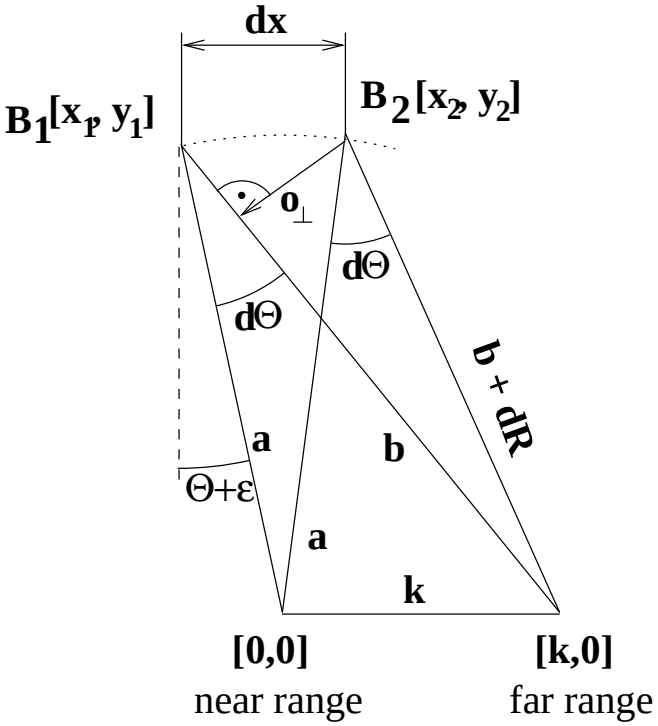

Figure 6.6: Illustration of the orbit adjustment.

and the difference dx between the two points may be derived:

$$dx = x_2 - x_1 = -\frac{bdR - \frac{dR^2}{2}}{k}. \tag{6.6}$$

Because $b \gg dR$, we can simplify the equation to

$$dx = -\frac{bdR}{k}. \tag{6.7}$$

If the baseline adjustment is small, i.e. $dR \ll b$, the direction of the adjustment is perpendicular to the radar ray (at near range).

The perpendicular baseline adjustment then looks like (see figure 6.6)

$$o_\perp = \frac{dx}{\cos(\Theta + \varepsilon)} = -\frac{bdR}{k\cos(\Theta + \varepsilon)}. \tag{6.8}$$

If the residual fringe frequency is df, then the phase of the interferogram at far range is $df \cdot d\Theta$. This means that the distance between the far-range point and the slave satellite should be corrected by

$$dR = -\frac{\lambda}{4\pi} df d\Theta. \tag{6.9}$$

The distance k between the near-range and far-range point is approximately $k = \frac{b \cdot d\Theta}{\cos(\Theta+\varepsilon)}$, resulting in

$$o_\perp = \frac{\lambda}{4\pi} df = dB_\perp. \tag{6.10}$$

That means that the baseline is corrected in the right direction. An approximation have been made during the derivation: $b \gg dR$ has almost no influence. Of course, as discussed in chapter 4, the frequency is not constant throughout the interferogram; on the other hand, the perpendicular component of the error baseline (and the baseline adjustment, too) is not constant either.

Book [12] (figure 6.4) is probably wrong in the sign of the slave slant range adjustment. In addition, the change of the parallel baseline between the near and far range corresponds to the perpendicular baseline (absolute value), because

$$n_\perp = \frac{dn_\parallel}{d\Theta}, \tag{6.11}$$

i.e.

$$\delta n_{||} \approx n_\perp \delta\Theta, \tag{6.12}$$

where $\delta\Theta$ is the difference in the look angle between the near and far range.

As described in section 4.6, the azimuth fringes are caused by a change in the baseline error and their number is usually neglectable. The error may be corrected with the procedure described in section 6.2.1. However, we propose another method: if we perform the baseline adjustment for enough lines in the interferogram, the azimuth fringes do disappear because the error baseline should be zero for all the lines of the interferogram.

6.2.4 Practical background of the procedure

The approach of adjusting baseline parameters with respect to the residual fringes requires the coordinates of the scene corners to be known, as well as the actual coordinates of both satellites. DORIS only allows us to know the satellite coordinates in a predefined time (for other timings, it may be interpolated).

The coordinates of the scene corners may be obtained from a different source (another geocoded image, map etc.). If geocoding in DORIS, the same satellite parameters are used, causing error. In addition, the orbits must be first corrected for the along-track and across-track errors (the large values, causing the scene shift).

Of course, the procedure may be iterated. Unfortunately, we are unable to try this approach, therefore we cannot say if the procedure converges or not.

6.2.5 Approach described in [28]

Paper [28] proposes to find the baseline parameters using a different method, based on the same principle. In the authors' words:

The baseline and slant range vectors

$$\vec{B_i} = B_{n,i}\vec{n} + (B_{c,i}\vec{c} + \alpha t_i)\vec{c}, \tag{6.13}$$
$$\vec{r_i} = r_{n,i}\vec{n} + r_{c,i}\vec{c}, \tag{6.14}$$

where t_i represents the time at which the point was acquired (relative to mid-scene). The coefficient α is used to model the baseline's across-track azimuth convergence (caused by non-parallel orbits), while $B_{n,i}$ and $B_{c,i}$ represent respectively the normal and cross-track components of the baseline at the mid-scene. (Vectors $\vec{n}$ and $\vec{c}$ denote the radial and across-track components of the orbit, respectively. The slant range vectors are related to the master satellite.)

The phase unwrapping procedure provides the interferometric phase Φ_i up to an unknown constant Φ_c. (...) One can construct a linear model for the phase difference:

$$\Phi_i = \frac{4\pi}{\lambda}\frac{\vec{r_i}\vec{B_i}}{|\vec{r_i}|} - \Phi_c. \tag{6.15}$$

Using the expressions for the look vector and baseline (equations (6.13) *and* (6.14)*) one then has:*

$$\Phi_i - \frac{4\pi}{\lambda}r_{n,i}B_{n,i} = \begin{bmatrix} \frac{4\pi}{\lambda}r_{c,i} & \frac{4\pi}{\lambda}r_{c,i}t_i & -1 \end{bmatrix} \begin{bmatrix} B_c \\ \alpha \\ \Phi_c \end{bmatrix}. \tag{6.16}$$

Three tie points allow one to create a system of equations that can be inverted to solve for the model parameters. The three tie points used to solve the system of equations would be well-distributed across the scene to avoid singularities. Improved accuracy can be obtained by using more tie points, and performing a non-linear least squares (LS) fit using the iterative Levenberg-Marquadt algorithm.

Comments

This procedure uses a different notation: in formula (6.15), the expression $\frac{\vec{r_i}\vec{B_i}}{|\vec{r_i}|}$ denotes the parallel baseline, different for each range pixel.

In comparison to previous approaches, this approach approximates the vertical baseline by a constant, and the horizontal baseline by a linear function. In case of more tie points, both of them may be approximated by a more complicated function, which must be expressed explicitly.

Also, let us write here the "correct" version of formula (6.16) (according to formula (6.15):

$$\Phi_i - \frac{4\pi}{\lambda}\frac{r_{n,i}B_{n,i}}{r_i} = \begin{bmatrix} \frac{4\pi}{\lambda}\frac{r_{c,i}}{r_i} & \frac{4\pi}{\lambda}\frac{r_{c,i}}{r_i}t_i & -1 \end{bmatrix} \begin{bmatrix} B_c \\ \alpha \\ \Phi_c \end{bmatrix}, \tag{6.17}$$

allowing to be written as

$$\Phi_i - \frac{4\pi}{\lambda}\cos\Theta_i B_{n,i} = \begin{bmatrix} \frac{4\pi}{\lambda}\sin\Theta_i & \frac{4\pi}{\lambda}\sin\Theta_i t_i & -1 \end{bmatrix} \begin{bmatrix} B_c \\ \alpha \\ \Phi_c \end{bmatrix}. \tag{6.18}$$

Let us stress here that the parameter α does not mean baseline orientation, but track convergence.

In equations (6.17) and (6.18), all of the Θ_i, r_i, $r_{c,i}$ and $r_{n,i}$ must be computed first. Although it may seem that the slant range r_i is known, the precision of the value is much worse (the slant range pixel size is about 10 m).

In addition, equations (6.16), (6.17) and (6.18) assume that the vertical baseline is correct, i.e. that its error is much smaller than that of the horizontal component.

If we also wish to adjust he vertical component, equation (6.18) should be rewritten to

$$\Phi_i = \begin{bmatrix} \frac{4\pi}{\lambda}\cos\Theta_i & \frac{4\pi}{\lambda}\sin\Theta_i & \frac{4\pi}{\lambda}\sin\Theta_i t_i & -1 \end{bmatrix} \begin{bmatrix} B_n \\ B_c \\ \alpha \\ \Phi_c \end{bmatrix}, \tag{6.19}$$

allowing for the non-linear adjustment as suggested in [28], because of the different precision of the vertical and horizontal baseline components.

6.3 Comparison of the methods

There are three important differences between these two methods and the `cpxdetrend` script:

- For `cpxdetrend`, no coordinates are needed. For the other methods, some tie points are required.
- The methods in [18] and [28] allow to correct the baseline parameters and geocode the image.
- `Cpxdetrend` is a simple approach, applicable for small scene crops because it approximates the residual phase by a linear function. In addition, the number of fringes can be only determined as an integral value; the fraction must be estimated.

The differences between the approaches suggested in [18] and [28] are the following:

- The procedure suggested in [18] is simpler and more illustrative; however, it does not allow to consider the precision of each baseline component.
- The procedure suggested in [18] considers only four tie points and the baseline parameters only at the first and last line of the scene. However, the scene may be split into parts and the baseline parameter adjustment may be performed for more tie points. On the other hand, [28] allows to approximate the baseline parameters by an explicit function.

- The procedure suggested in [28] also finds the phase-unwrapping constant Φ_c, which is probably not useful any more.
- While procedure suggested in [18] requires the actual distance between the satellites and the tie points to be known, the procedure suggested in [28] requires only the knowledge of the look angle Θ for each pixel.

6.4 Geocoding the original scene using tie points

It is difficult to geocode the slant-range image using tie points. We tried to geocode the magnitude image with the help of a geocoded Landsat optical image, covering a large part of the radar scene (however, it was not the entire scene). In addition to different scattering features of both signals (although water is almost perfectly "black" in the optical images, it is not the case of the radar images because of imperfect SAR processing), the pixel length (in the range direction) is not constant throughout the image (at close range, the pixels are about 50% longer than those at far range). The analytical form of the transformation is

$$x = \sqrt{z^2 - h^2}, \tag{6.20}$$

where z is the slant range (i.e. the position of a point in the radar image, x is the ground range (i.e. the position of a point in an optical image) and h is the height of the satellite. Let us approximate formula (6.20) with a polynomial

$$z - z_0 = a_0 + a_1(x - x_0) + a_2(x - x_0)^2 + \ldots + a_n(x - x_n)^n + \mathcal{O}_{n+1}, \tag{6.21}$$

where $\mathcal{O}_{n+1}$ is the maximum approximation error of the polynomial of the order n, x_0 and z_0 are the coordinates of the scene center (ground and slant range) and

$$a_i = \frac{1}{i!}\frac{d^i z}{dx^i} \text{ for } i = 1,\ 2,\ \ldots\ n. \tag{6.22}$$

The term a_0 corresponds to the shift between the images and is not considered here. For the case of formula (6.20), these coefficients can be expressed as

$$a_1 = \frac{x}{\sqrt{x^2 + h^2}}, \tag{6.23}$$

$$a_2 = \frac{1}{2}\frac{h^2}{(x^2 + h^2)^{\frac{3}{2}}}, \tag{6.24}$$

$$a_3 = -\frac{h^2}{2}\frac{x}{(x^2 + h^2)^{\frac{5}{2}}}, \tag{6.25}$$

$$a_4 = -\frac{h^2}{8}\frac{(h^2 - 4x^2)}{(x^2 + h^2)^{\frac{7}{2}}}, \tag{6.26}$$

$$a_5 = \frac{h^2 x}{8}\frac{3h^2 - 4x^2}{(x^2 + h^2)^{\frac{9}{2}}}, \tag{6.27}$$

$$\mathcal{O}_n = |a_n|\, dx^n, \tag{6.28}$$

etc.

For evaluation of these coefficients (and the residual errors), we need to know that $x \approx 250$ km, $dx \approx 50$ km (half of the scene), $h \approx 780$ km. The evaluated maximum approximation errors are shown in table 6.1.

order n	$a_n[\mathrm{m}^{-n+1}]$	$\mathcal{O}_n[\mathrm{m}]$
1	0.30	1500
2	0.55e-3	1375
3	-2.1e-7	26
4	-1.1e-10	0.69
5	1.8e-13	0.056

Table 6.1: The coefficients of the polynomial and the maximum error of the polynomial approximation.

It can be seen from table 6.1 that the second-order polynomial approximation is sufficient for scenes where one pixel is 20 to 30 m long. In addition, the tie points cannot be determined with such a high precision of one pixel, because of the imperfectly focused radar images. The distribution of tie points is not perfect due to the fact that only large water surfaces are detectable in the radar magnitude image.

Results

For geocoding, 9 tie points were used, their distribution was not optimal, however. Only approximately half of the crop was covered, due to the reasons cited above. The transformation residual RMS was 11.95 pixels in the range direction and 0.76 pixels in the azimuth direction for the first-order polynomial approximation, and 3.95 pixels in the range direction and 3.21 pixels in the azimuth direction for the second-order polynomial approximation. The PCI Geomatica software does not allow different transformation in each direction. The scene crop was then transformed using the second-order polynomial approximation.

However, the RMS of the residuals depends largely on the size of the crop to be geocoded; for large scenes, the RMS error is much larger.

method	orbits (DORIS)		tie points		difference	
corner	$Y[m]$	$X[m]$	$Y[m]$	$X[m]$	$Y[m]$	$X[m]$
north-east	753 975	972 720	741 087	958 587	12 888	14 133
south-east	778 344	1 032 872	764 249	1 009 226	14 095	23 646
south-west	855 807	1 002 636	815 669	989 248	40 138	13 388
north-west	831 967	942 419	792 567	938 665	39 400	3 754

Table 6.2: The geocoding difference between using tie points (in a slant-range image) and DORIS geocoding for the topo pair. Geocoding using tie points was performed in PCI Geomatica software. The coordinates are in the S-JTSK coordinate system.

However, geocoding of the image using tie points does not allow us to get heights. The (unwrapped) interferogram phase does not correspond to the height directly, it represents the distance between the place on the Earth and the satellite; in order to get the height, it must be converted (the look angle is different for different pixels).

6.5 Direct geocoding

In DORIS, geocoding is computed with the use of satellite positions. In fact, there is no other way to perform slant-range to ground-range conversion. However, this is not precise due to the errorneous satellite positions, and we decided to compare the geocoded image to the same LandSat image as in the last section.

For conversion from the radar to the geographic system, the height of a point above the ellipsoid must be known (at least approximately). DORIS only allows to geocode an interferometric DEM; at the same time, all other images (magnitude, differential interferogram, coherence) are geocoded. But if the unwrapped interferometric DEM does not exist, the problem is much more complicated.

Let us stress here that geocoding with no DEM at all cannot be performed or would be very inaccurate. We can also use an external DEM (e.g. SRTM) but in that case we need to shift the DEM in order to compensate for the interferogram shift (see section 5.3) and then consider this to be the created DEM and use it for geocoding.

The shift of the DEM cannot be determined to a precision of a pixel; but depending on the height ambiguity, the error does not have to cause a large geocoding error, especially in a flat terrain.

However, this approach is not as clear as regular geocoding, i.e. geocoding using the height from the unwrapped interferogram. The differences are following:

- the interferogram was constructed from the scenes and therefore the correct values of satellite orbits apply, while the interferogram simulation (radarcoding) was performed using the known orbits;
- the interferogram unwrapping may have failed and geocoding can never be performed well for the case of the classical interferogram;
- even if unwrapping succeeded, there is no way to determine the initial height value of a pixel; i.e. the unwrapped phase may be shifted by an integer multiple of 2π without any consequences; this causes that all the interferogram heights are shifted by an integer multiple of height ambiguity.

The described approach uses the known satellite orbits and it only helps to correct the along-track orbits (but the precision of the correction is not sufficient for interferogram improvement). Across-track and radial orbits may be corrected too, but they are also used for interferogram creation and height ambiguity computations.

Results

The geocoded scene was compared to a previously geocoded LandSat scene in order to see the influence of the orbit errors on the geographical coordinates. However, we were not able to geocode the entire crop displayed, e.g., in figure 5.1, but only a part of it, 1000 pixels in both directions (i.e. 5000 pixels in azimuth of the original scene). The coordinates are shown in table 6.3, the situation is illustrated in figure 6.7.

As noted above, the magnitude image itself is not sharp, and its sharpness was further damaged by resampling (within transformation from slant range to WGS-84 and then to S-JTSK). We therefore estimate the precision of the radar coordinates not to be worse than 200 m.

	LandSat scene		DORIS geocoding		difference		
point	Y[m]	X[m]	Y[m]	X[m]	Y[m]	X[m]	total [m]
1	761,248	990,738	761,149	986,280	-99	-4458	4459
2	762,845	988,646	762,429	984,480	-416	-4166	4187
3	780,107	978,546	779,589	974,620	-518	-4226	4258
4	772,720	975,411	772,269	971,120	-451	-4219	4243
5	781,337	980,464	781,309	975,280	-28	-5184	5184
6	759,357	980,590	759,229	976,000	-128	-4590	4592

Table 6.3: The geocoding errors for the defo 2 pair. All values are in the S-JTSK coordinate system.

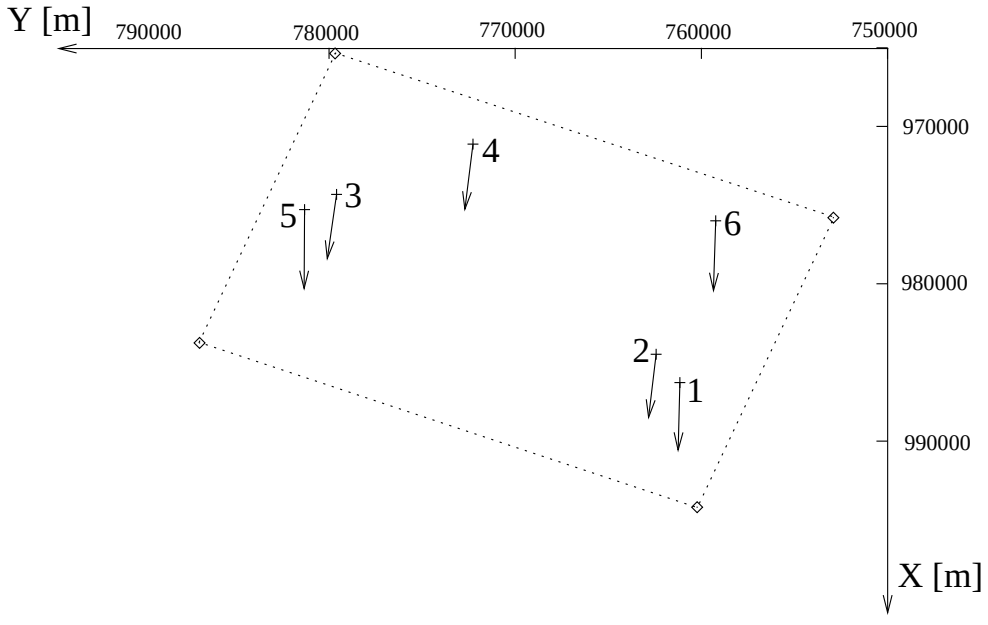

Figure 6.7: Illustration of the tie points in the scene crop. Crosses denote the radar-geocoded points, the arrows aim at the correct point. The bullets denote the crop corners.

Please note that the originally (in slant range) almost squarish scene is now elongated.

In figure 6.7, one can clearly see that the scene is mostly shifted in the azimuth direction, i.e. the shift is caused by the along-track orbit error.

Table 6.4 shows the shift of the tie points (defined in table 6.3) in the azimuth-range coordinates. The azimuth direction was computed from the coordinates of the scene crop corners (average between the direction in close range and far range), $\sigma_{az} = 201.64\,°$.

point	azimuth shift [m]	range shift [m]
1	4107	1736
2	3719	1923
3	3737	2040
4	3755	1975
5	4808	1938
6	4219	1812
average	4058	1904

Table 6.4: The tiepoint shifts from table 6.3 converted to the azimuth-range coordinate system.

It may be seen from table 6.4 that the along-track error, projected on the Earth surface, is about 4 km.

The range error may be caused by both across-track and radial orbit errors. A little part of it may be also caused by a DEM error (there are holes in the DEM which we did not interpolate) but this can only be attributed to the variance.

Rather than by orbit errors, the shift in the range direction may be caused by a small rotation of the satellite with respect to the value of look angle Θ for which processing was performed: for the distance of 850 km, the shift of 1900 m corresponds to 0.13°. However, we have no information about the tolerance and precision of the rotation recording.

That means that after geocoding in DORIS, the scene should be geocoded once more using tie points. Here, linear transformation is sufficient.

Chapter 7

Conclusions

The thesis has analysed the influence of orbit errors on interferograms. Not only the two scenes are shifted with regard to each other and the interferogram is shifted with respect to a DEM, but the interferogram also looks sloped. This is the most important influence for deformation mapping, because the long-wave phase change caused by the orbit errors may make the places of deformation wrongly visible in the interferogram.

The orbit errors are partly caused by improper modeling of the Earth gravity field, and partly by improper model of satellite geometry. While the error in the Earth gravity field only causes the geographically-dependent orbit errors, the errors in the modeling of the atmospheric drag and solar radiation pressure influence on the satellite cause errors which are geographically independent, i.e. they differ in different passes above a given area. These are the errors which have impact on the interferograms.

The influence depends not only on the size of the orbit errors, but also on the orientation of the error vector which can not be estimated in advance, in contrast to its length. For three-pass interferometry, the difference between the error vectors is even more important than their own lengths and orientations. The influences of the orbit errors are reduced if $0 < p < 1$ (p is the ratio of the perpendicular baselines of the two pairs), otherwise they are added up. It is clear that the three-pass interferometry is the best method to reduced the orbit error influence, although it is not always possible (due to the limited data amount).

On the other hand, the residual interferogram slope may be used to correct for the orbit errors in the radial and across-track directions. However, due to the fact that the interferogram is only a difference between two acquired scenes, it is not possible to correct both satellite tracks – we are only able to use the interferogram slope to correct the baseline – its horizontal and vertical components.

The shift of the scenes with regard to each other may be used to correct the along-track orbit error (timing error), which is the largest of all the components. However, it is again only possible to correct it relatively to the master satellite track.

The shift of the processed interferogram with regard to the reality is caused mostly by the master-satellite orbit error. This is the only measure of the orbit error of the master satellite. Knowing the shift, we are able to correct for the along-track error, which is probably larger than a few decimeters. However, the shift of the scene in the range

direction is probably caused not only by the radial and across-track components of the orbit error, but also by a wrong value of the look angle Θ with which it is processed.

Unfortunately, we are now unable to correct for the orbit errors influence, except for the simple and imprecise `cpxdetrend` script. The other ways, which allow to adjust the baseline length and orientation, are only analysed theoretically and will be the subject of our future work (see the following chapter).

Chapter 8

Future work

In the future, we would like to continue our work dealing with the orbit adjustment with respect to residual fringes in the interferogram.

A disadvantage of all the cited methods to eliminate the residual fringes is that the residual phase or fringe frequency must be estimated manually, there is no possibility to compute it automatically (except for FFT, which is discrete).

We would like to develop a method for automatic adjustment of the orbits, based on phase coregistration of the interferogram and a radarcoded (external) DEM. The first (and probably the most important) reason for that is that it should improve the existing coregistration, which must be estimated manually and does not allow to shift the DEM by a non-integral number of pixels, causing artifacts in the image.

The coregistration procedure consists of three steps:

- shift vector determination in some points of the image,
- approximation of these vectors by a continuous function,
- resampling of the image.

For the second and third step, we plan to use the functions already implemented in DORIS. The only procedure to be implemented is the shift vector determination.

Phase coregistration is not as straightforward as the magnitude coregistration. There are two basic reasons for that:

- the phase is wrapped, e.g. values which, mathematically, seem to be far away from each other, may be actually very close,
- the phase difference between the interferogram and the radarcoded DEM may be non-zero and slowly changing.

It is not adviceable to unwrap the phase before phase coregistration: phase unwrapping may cause significant errors. We suggest the following procedure to perform phase coregistration:

1. Suppose we know an approximate shift vector (with the precision of 10 pixels).
2. The interferogram is split into many small parts (e.g. 100 pixels in each direction) and each part is processed independently.
3. The optimal shift between a given part and the corresponding crop of the radarcoded DEM is found. One of the images is shifted in order to exactly overlap with the other.
4. The exactly overlapping parts of the images (interferogram and DEM) are subtracted from each other. The result is a difference image and should be a little sloped (in correlated areas).
5. An approximate slope of the entire image is evaluated; it may be combined from two factors: the slopes of the small parts of the image (if the slope is large) or the difference between the mean phase values of the small difference images in different parts of the entire image (if the slope is not large enough to be recognized in the small image). However, it is neccessary to perform phase unwrapping here, we hope that the errors will not propagate to the entire-scene values.
6. The mean value of the difference phase, determined from coherent areas, is subtracted from the small crops of the interferogram.
7. The computed slope (for the entire scene) is also subtracted from the small crops of the interferogram.
8. The interferogram is reconstructed and shift vector estimation is performed once more.
9. The slope of the interferogram (evaluated in different parts) serves for orbit adjustment, performed using either of the methods described in section 6.2.

During the computations, the small parts of the images are to be oversampled in order to make the shifts more accurate.

A disadvantage of this procedure is that the approximate shift must be known in advance, i.e. it must be estimated manually. However, the interferogram and the DEM are better coregistered, allowing to eliminate the artifacts from the interferograms.

An advantage of this procedure is that it performs geocoding at the same time (it assigns each pixel of the interferogram to a pixel in the radarcoded DEM which is computed using the geocoded DEM).

This procedure is correct if the DEM is radarcoded with use of the correct baseline parameters; therefore, these must be at least approximately known in advance. We hope that the method converges.

Software and Data Used

Software

For interferogram creation, we use the open-source software DORIS (Delft Object-oriented Radar Interferometric Software), developed at TU Delft [15].

Phase unwrapping is performed in the open-source SNAPHU (Statistical-Cost Network-Flow Algorithm for Phase Unwrapping) program. This program is implemented as described in [2, 3, 4].

For graph computation and plotting, we use the open-source software OCTAVE and GNUPLOT.

For detrending the interferogram, we use the `cpxdetrend` script, also developed at TU Delft, to be run under MATLAB.

For DEM data handling, we use open-source GRASS GIS (Geographic Resources Analysis Support System), originally developed at U.S. Army Construction Engineering Research Laboratories, now developed by the world-wide community.

For conversion of individual points between the S-JTSK and WGS-84 coordinate systems, the MatKart software, developed at the Department of Mapping and Cartography, the Czech Technical University, is used.

However, conversion of the entire scene crop (section 6.5) was performed in the ArcInfo software.

Data

Three SAR scenes were processed, acquired at March 7^{th}, 1999 (ERS-1), March 8^{th}, 1999 (ERS-2) and December 28^{th}, 1998 (ERS-2), all of them at orbit no. 20288. Data were provided by ESA through a category-1 project.

As an external DEM, we use the SRTM DEM acquired by the Shuttle Radar Topography Mission [21] in February 2000.

For data geocoding, an optical image of a similar locality acquired by Landsat TM in 1998 was used. Geocoding of the image was performed using a map at 1:50,000 scale.

Bibliography

[1] A. Arnaud, N. Adam, R. Hanssen, J. Inglada, J. Duro, J. Closa, and M. Eineder. ASAR ERS interferometric phase continuity. In *igarss03*, 2003.

[2] C. W. Chen and H. A. Zebker. Network approaches to two-dimensional phase unwrapping: intractability and two new algorithms. *Journal of the Optical Society of America A.*, 17(3):401–414, mar 2000.

[3] C. W. Chen and H. A. Zebker. Two-dimensional phase unwrapping using statistical models for cost functions in nonlinear optimization. *Journal of the Optical Society of America A.*, 18:338–351, feb 2000.

[4] C. W. Chen and H. A. Zebker. Phase unwrapping for large SAR interferograms: statistical segmentation and generalized network models. *IEEE Transactions on Geoscience and Remote Sensing*, 40(8):1709–1719, aug 2002.

[5] J. Closa. The influence of orbit precision in the quality of ERS SAR interferometric data. Technical Report ES-TN-APP-APM-JC01, ESA, 1998.

[6] A brief overview of DORIS system evolutions. http://ids.cls.fr/html/report/ids_workshop_2002/PS_DORIS_IDS2002.pdf.

[7] ENVISAT instruments. http://envisat.esa.int/instruments/.

[8] Eoportal directory: ERS-2. http://directory.eoportal.org/.

[9] ERS mission phases. http://www.deos.tudelft.nl/ers/phases/.

[10] F. Gatelli, A. Monti Guarnieri, F. Parizzi, P. Pasquali, C. Prati, and F. Rocca. The wavenumber shift in SAR interferometry. *IEEE Transactions on Geoscience and Remote Sensing*, 32(4):855–865, jul 1994.

[11] D. C. Ghiglia and M. D. Pritt. *Two-dimensional phase unwrapping: theory, algorithms, and software.* John Wiley & Sons, Inc, New York, 1998.

[12] R. F. Hanssen. *Radar Interferometry: Data Interpretation and Error Analysis.* Kluwer Academic Publishers, Dordrecht, 2001.

[13] M. Jehle, O. Frey, D. Small, E. Meier, and D. Nesch. Improved knowledge of SAR geometry through atmospheric modelling. In *eusar2004*, pages 909–911, 2004.

[14] B. Kampes. DORIS manual. http://enterprise.lr.tudelft.nl/doris/usermanual/.

[15] B. M. Kampes, R. F. Hanssen, and Z. Perski. Radar interferometry with public domain tools. In *fringe03*, page 6 pp., 2003.

[16] J. Klokočník. Lectures in cosmic geodesy 21.

[17] J. Kostelecký. Lectures in cosmic geodesy 11.

[18] D. Massonnet and K. L. Feigl. Radar interferometry and its application to changes in the earth's surface. *Reviews of Geophysics*, 36(4):441–500, nov 1998.

[19] Satellite laser ranging data. http://www.deos.tudelft.nl/ers/operorbs/node8.html.

[20] ERS and ENVISAT precise orbit determination. http://www.deos.tudelft.nl/ers/precorbs/.

[21] B. Rabus, M. Eineder, A. Roth, and R. Bamler. The shuttle radar topography mission—a new class of digital elevation models acquired by spaceborne radar. *ISPRS Journal of Photogrammetry and Remote Sensing*, 57:241–261, 2003.

[22] G. W. Rosborough. Satellite orbit perturbations due to the geopotential. 1986.

[23] ERS instruments. http://www.deos.tudelft.nl/ers/instruments.html.

[24] ERS operations. http://earth.esa.int/ers/eeo4.39/.

[25] Satellite sensors. http://www.ga.gov.au/acres/prod_ser/radadata.htm.

[26] R. Scharroo and P. Visser. Precise orbit determination and gravity field improvement for the ERS satellites. *Journal of Geophysical Research*, 103(C4):8113–8127, 1998.

[27] R. Scharroo and P. N. A. M. Visser. ERS tandem mission orbits: is 5 cm still a challenge? In *Proceedings of the Third ERS Symposium*, 1997.

[28] D. Small, C. Werner, and D. Nüesch. Baseline modelling for ERS-1 SAR interferometry. In *igarss93*, pages 1204–1206, 1993.

[29] H. Tarayre and D. Massonnet. Effects of refractive atmosphere on interferometric processing. In *igarss94*, pages 717–719, 1994.

[30] H. Tarayre and D. Massonnet. Atmospheric propagation heterogeneities revealed by ERS-1 interferometry. *Geophysical Research Letters*, 23(9):989–992, may 1996.

[31] U. Wegmüller. Automated terrain corrected SAR geocoding. In *igarss99*, pages 1712–1714, 1999.